| OCRWM | DESIGN CALCULATION OR ANALYSIS COVER SHEET | 1. QA: QA<br>2. Page 1 |
|---|---|---|

| 3. System | 4. Document Identifier |
|---|---|
| Uncanistered Spent Nuclear Fuel | 000-00C-DSU0-02200-000-00A |

5. Title

Drop of Waste Package on Emplacement Pallet - A Mesh Study

6. Group

Analyses and Component Design

7. Document Status Designation

☒ Preliminary ☐ Final ☐ Cancelled

8. Notes/Comments

An interdisciplinary review was completed on 04 September 2003.

| Attachments | Total Number of Pages |
|---|---|
| List of attachments is presented in Section 8 | |
| | |
| | |
| | |

RECORD OF REVISIONS

| 9. No. | 10. Reason For Revision | 11. Total # of Pgs. | 12. Last Pg. # | 13. Originator (Print/Sign/Date) | 14. Checker (Print/Sign/Date) | 15. QER (Print/Sign/Date) | 16. Approved/Accepted (Print/Sign) | 17. Date |
|---|---|---|---|---|---|---|---|---|
| 00A | Initial Issue | 61 | VII-4 | Sreten Mastilovic<br>04 SEP. 2003 | Valerie de la Brosse<br>9/6/03<br>9/5/03 VdB | Daniel J. Tunney<br>9/5/2003 | Michael J. Anderson | 9/6/03 |

# CONTENTS

# FIGURES

Page



# TABLES

Page

## 1. PURPOSE

The objective of this calculation is to study mesh sensitivity of the results evaluated for a waste package (WP) outer corrosion barrier (OCB) during the impact between the WP and an emplacement pallet (hereinafter referred to as the pallet). The results selected for this purpose are the maximum stress intensity in the WP OCB during the impact and the area of the WP OCB where the residual 1st principal stress exceeds a certain limit. (The area of the WP OCB where the residual 1st principal stress exceeds the stress limit is hereinafter referred to as "the damaged area" with the exception of Attachment V.) The stress limit (damage threshold) is defined as a fraction of the yield strength of the OCB material, Alloy 22 (SB-575 UNS N06022 hereinafter referred to as Alloy 22), at given temperature. Two stress limits (lower and upper) used throughout this document are defined as 80 percent and 90 percent, respectively, of yield strength of Alloy 22 (see Assumption 3.9) at temperature of 150 *°C*.

The scope of this document is limited to:

1. Reporting the damaged area
2. Reporting the calculation results in terms of maximum stress intensity in the course of transient simulation
3. Analyzing the results with respect to the finite element (FE) mesh size.

This calculation is associated with the WP design and is performed by the Analyses and Component Design group. AP-3.12Q, *Design Calculations and Analyses* (Ref. 1) is used to perform the calculation and develop the document. The WP is classified as Quality Level 1 (Ref. 5, p. 7). Therefore, this calculation is subject to *Quality Assurance Requirements and Description* (Ref. 4).

The design of the 21-PWR (Pressurized Water Reactor) WP used in this calculation is defined in Reference 24; the exceptions are the radial gap between the inner vessel and the OCB (for which a value of 4 *mm* is used [Ref. 25, Section 8.1.8]) and the OCB thickness (for which a value of 18 *mm* is assumed [Assumption 3.10]). The sketch in Attachment I provides additional information not included in Reference 24. (Note that this calculation is performed for the baseline Site Recommendation design, instead of the most recent 21-PWR WP design, since it supports previously performed calculations of the WP exposed to vibratory ground motion [presented in Ref. 16] that are performed for the baseline design.) Also note that the WP components indicated as "inner shell" and "outer shell" in Attachment I and Reference 24 are hereinafter called "inner vessel" and "outer corrosion barrier", respectively.) Design of the pallet used in this calculation is defined in Reference 22; the sketch in Attachment II provides additional information not included in Reference 22 (see also Assumption 3.13). All obtained results are valid for these designs only.

## 2. METHOD

The FE mesh is created by using the commercially available ANSYS V5.6.2 FE code (Software Tracking Number [STN] 10364-5.6.2-01, Ref. 6). The FE calculations are then performed by using the commercially available LS-DYNA V960.1106 (STN 10300-960.1106-00, Ref. 7) FE code. The results of this calculation are provided in terms of damaged area and maximum stress intensity.

## 3. ASSUMPTIONS

In the course of developing this document, the following assumptions are made regarding the structural calculation.

3.1 Some of the temperature-dependent material properties (specifically: density and Poisson's ratio) are not available for Alloy 22 and SA-240 S31600 (hereinafter referred to as 316 stainless steel [SS]) except at room temperature (RT) (20 °C). The RT density and RT Poisson's ratio are assumed for both materials. The impact of using RT density and RT Poisson's ratio is anticipated to be small. The rationale for this assumption is that the material properties in question do not have dominant impact on the calculation results. This assumption is used in Sections 5.1 and 5.1.1 and corresponds to Section 5.2.8.4 of Reference 8.

3.2 The temperature-dependent material properties are not available for TSw2 (Topopah Spring Welded-Lithophysal Poor) rock except at RT. The corresponding RT material properties are assumed for this material. The impact of using RT material properties is anticipated to be small. The rationale for this assumption is that the material properties of the rock do not have an impact on the calculation results. This assumption is used in Sections 5.1 and 5.1.1.

3.3 Some of the strain-rate-dependent material properties are not available for Alloy 22 at any strain rate. The material properties obtained under the static loading conditions are assumed for Alloy 22. The impact of using material properties obtained under static loading conditions is anticipated to be small. The typical maximum strain rate in the WP OCB observed in this calculation is 55 $s^{-1}$ (as indicated by maximum slope of the effective-strain time history, see Figure 1). The rationale for this assumption is that the mechanical properties of ductile materials do not significantly change at the peak strain rates that occur during the drop simulation (Ref. 14, Figures 27 and 30). Furthermore, this is primarily a mesh study and the objective should not be significantly affected by the relatively small variations of mechanical properties due to strain rate. This assumption is used in Section 5.1 and corresponds to Section 5.2.5 in Reference 8.

3.4 The Poisson's ratio of Alloy 22 is not available in literature. The Poisson's ratio of Alloy 625 (SB-443 N06625) is assumed for Alloy 22. The impact of this assumption is anticipated to be negligible. The rationale for this assumption is that the chemical compositions of Alloy 22 and Alloy 625 are similar (see Ref. 9, Table "Chemical Composition in Weight %" and

Ref. 10, p. 143, respectively). This assumption is used in Section 5.1 and corresponds to Section 5.2.8.2 of Reference 8.

3.5 The modulus of elasticity and Poisson's ratio of the TSw2 are characterized by a significant scatter of data (see Ref. 28, Tables 3 and 4, respectively). For the purpose of the present calculation, modulus of elasticity is assumed to be 33 *GPa*, and Poisson's ratio 0.21. The rationale for this assumption is that these values agree with typical values of said properties for most rocks of interest (see Ref. 28, Tables 3 and 4). The modulus of elasticity and Poisson's ratio of the TSw2 are used in this calculation only to represent the contact properties of the invert (which is represented as a rigid part). The said properties, therefore, have a negligible effect on the WP OCB results presented in this calculation. This assumption is used in Section 5.1.

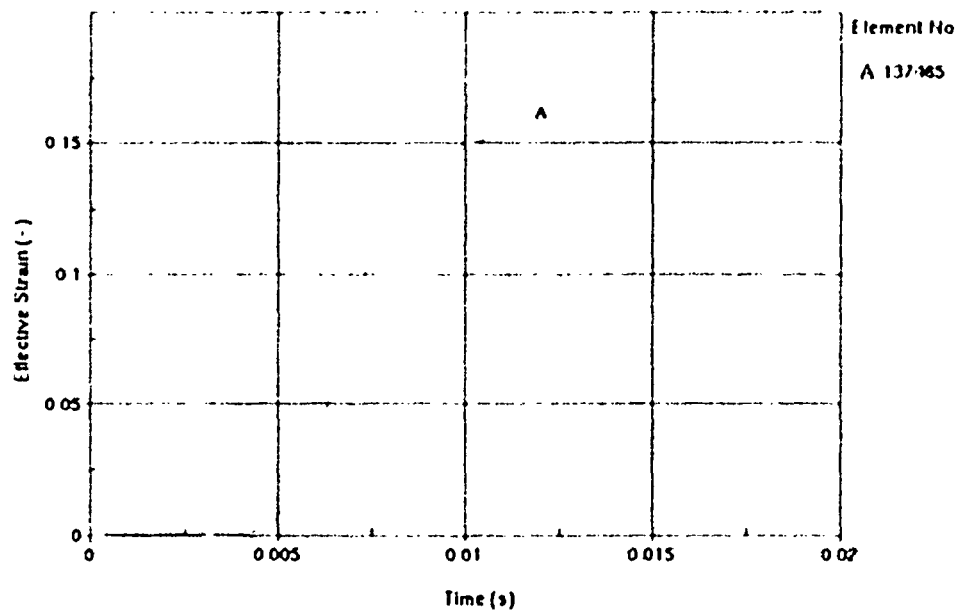


Figure 1 Effective Strain Time History (Detail) for Element 137465 Characterized by the Maximum Stress Intensity Among the OCB Elements (5-*m/s* Horizontal Drop with Mesh 4)

3.6 The density of the TSw2 is assumed to be $2370 kg/m^3$. The rationale for this assumption is that this value agrees well with all Topopah Spring Welded rocks and is not exceeded by any of the other rocks presented in Reference 23 (Table 2). It should be noted that this assumption has no effect on the calculation results since density of the rock affects only the mass of the rigid invert. This assumption is used in Section 5.1.

3.7 The exact geometry of the loaded internals is simplified for the purpose of this calculation. The WP inner vessel (including the inner vessel lids) and its internals (including the spent nuclear fuel [SNF]) are represented by a thick-wall cylinder of uniform thickness and circular cross section made from 316 SS (see Section 5.2). The thickness of this cylinder is determined by the cumulative mass of these components. The rationale for this assumption

is that the inner vessel internal structure and the SNF affect the results of this calculation predominantly through their mass and overall dimensions. This assumption is used in Section 5.2.

3.8 The uniform strain (strain corresponding to the ultimate strength on the stress-strain curve) of Alloy 22 is not available in literature. Therefore, it is conservatively assumed that the uniform strain is 90 percent of the elongation. The rationale for this assumption is the character of stress-strain curve for Alloy 22 (see Ref. 15). This assumption is used in Section 5.1.2 and corresponds to Section 5.2.8.6 of Reference 8.

3.9 The distribution of the residual stress threshold is assumed to be uniform with a lower bound of 80 percent of the yield strength of Alloy 22 and an upper bound of 90 percent of the yield strength of Alloy 22. The basis for this assumption is the data provided in Reference 29. This assumption is used in Section 1 and Attachment V.

3.10 The thickness of the WP OCB is reduced by 2 $mm$. The rationale for this assumption is discussed here. The OCB will degrade due to general corrosion during the regulatory period. The thickness reduction of 2 $mm$ over the regulatory period of 10,000 years corresponds to the general corrosion rate of $2 \cdot 10^{-4}$ $mm/yr$. This thickness reduction is used for seismic calculations (Ref. 16, Section 3) and is retained for consistency in the present FE mesh study. This assumption is used in Sections 1 and 5.2 and Attachment VII.

3.11 The friction coefficients for contacts among the Alloy 22 components, or for the contacts involving Alloy 22 and 316 SS, are not available in literature. It is, therefore, assumed that the dynamic (sliding) friction coefficient for both of these contacts is 0.55. The rationale for this assumption is that this friction coefficient is typical for most dry nickel-on-steel and nickel-on-nickel contacts (see Ref. 26 [Table 3.2.1, p. 3-26]), nickel being the dominant component in Alloy 22 (Ref. 9, Table "Chemical Composition in Weight %"). This assumption is used in Section 5.2.

3.12 The variation of functional friction coefficient between the static and dynamic value as a function of relative velocity of the surfaces in contact is not available in literature for the materials used in this calculation. Therefore, the effect of relative velocity of the surfaces in contact is neglected in these calculations by assuming that the functional friction coefficient and static friction coefficient are both equal to the dynamic friction coefficient. The impact of this assumption on results presented in this document is anticipated to be negligible. The rationale for this conservative assumption is that it provides the bounding set of results by minimizing the friction coefficient within the given FE-analysis framework. This assumption is used in Section 5.2 and corresponds to Section 5.2.14.4 of Reference 8.

3.13 The longitudinal pallet tubes (Tube 1 in Attachment II) are, for the purpose of this calculation, assumed to be made of Alloy 22. This assumption has a negligible impact on the calculation results. The rationale for this assumption is that due to the long-term

corrosion it is impossible to take structural credit for these tubes as long as they are made of 316 SS. This assumption is used in Sections 1, 5.1, and 5.2.

3.14 The temperature of the WP is assumed to be 150 °C for temperature-dependent material properties. The rationale for this assumption is that this temperature is conservative for most of the regulatory period for high-temperature operating modes (97 percent of the regulatory period [see Reference 21, Figure 6-3]) and strictly conservative for low-temperature operating modes. This assumption is used in Section 5.1.

3.15 The WP bottom and top ends are, for the purpose of FE representation, both based on the bottom-end configuration (see Attachment I and Reference 24). This simplification has no effect on the results, as obtained in this calculation. The rationale for this assumption is that it simplifies FE representation without affecting the calculation results. This assumption is used in Section 5.2.

## 4. USE OF COMPUTER SOFTWARE

One of the FE analysis computer codes used for this calculation is ANSYS V5.6.2, which is obtained from Software Configuration Management in accordance with appropriate procedure (Ref. 2), and is identified by STN 10364-5.6.2-01 (Ref. 6). ANSYS V5.6.2 is a qualified, commercially available FE code and is appropriate for application performed in this calculation. The calculations using ANSYS V5.6.2 software are executed on two Hewlett-Packard (HP) 9000 series UNIX workstations (Operating System HP-UX 11.00) identified with the YMP (Yucca Mountain Project) property tag numbers 151324 and 151325 located in Las Vegas, Nevada. The development of FE mesh by ANSYS is fully within the range of the validation performed for ANSYS V5.6.2 code. Access to the code is granted by the Software Configuration Management in accordance with the appropriate procedures.

The input files (identified by .inp file extension) and output files (identified by .out file extension) for ANSYS V5.6.2 are provided in Attachment VIII.

The qualified FE analysis computer code used for this calculation is Livermore Software Technology Corporation (LSTC) LS-DYNA V960.1106 (Ref. 7). LS-DYNA V960.1106 is obtained from Software Configuration Management in accordance with the appropriate procedure (Ref. 2) and is identified by STN 10300-960.1106-00. LS-DYNA V960.1106 is appropriate for this calculation. The LS-DYNA V960.1106 evaluation performed for this calculation is fully within the range of the validation performed for the LS-DYNA V960.1106 code. The calculations are executed on six HP 9000 series UNIX workstations (Operating System HP-UX 11.00) identified with the YMP property tag numbers 150688, 150689, 150690, 151691, 151664, and 151665 located in Las Vegas, Nevada. Access to the code is granted by the Software Configuration Management in accordance with the appropriate procedures.

The input files (identified by .k, .dat, and .inc file extensions) and output files (d3hsp, d3plot, d3thdt, and messag) for LS-DYNA V960.1106 are provided in Attachment VIII.

As identified in Section 6, LSPOST V2 (LSTC) is a postprocessor used for visual display and graphical representation of data that is exempt from the requirements defined in Reference 2 (Section 2.1.2).

The input and output ANSYS V5.6.2 and LS-DYNA V960.1106 files are archived by using WinZip V8.1 and submitted on compact discs as Attachment VIII (see Table 9). WinZip V8.1 belongs to the category of automated office support systems that is exempt from the requirements defined in Reference 2 (see Section 2.1.1).

# 5. CALCULATION

## 5.1 MATERIAL PROPERTIES

Material properties used in these calculations are listed in this section. The material properties are evaluated for 150 *°C* (Assumption 3.14). Some of the temperature-dependent and rate-dependent material properties are not available for Alloy 22, 316 SS, and TSw2 rock. Therefore, RT density and RT Poisson's ratio are used for Alloy 22 and 316 SS (see Assumption 3.1). RT material properties are used for TSw2 rock (Assumption 3.2). Finally, all mechanical properties used in this calculation are obtained under static tensile loading conditions (Assumption 3.3).

SB-575 N06022 (Alloy 22) (OCB, OCB lids, trunnion sleeves, and pallet [see Assumption 3.13])
(Note: All properties of Alloy 22 are obtained from Reference 9. However, while the density, Poisson's ratio, and modulus of elasticity are uniquely defined therein, the elongation and strengths are available in more than one table. The latter properties are, for the purpose of this calculation, obtained from Table "*Plate, $\frac{1}{4}-\frac{3}{4}$ in. (6.4 – 19.1 mm) thick*"):

Density = 8690 $kg/m^3$ (at RT)

Yield strength = 338 *MPa* (at 200 *°F* = 93 *°C*)
Yield strength = 283 *MPa* (at 400 *°F* = 204 *°C*)

Ultimate strength = 738 *MPa* (at 200 *°F* = 93 *°C*)
Ultimate strength = 676 *MPa* (at 400 *°F* = 204 *°C*)

Elongation = 0.65 (at 200 *°F* = 93 *°C*)
Elongation = 0.66 (at 400 *°F* = 204 *°C*)

Poisson's ratio = 0.278 (at RT) (Assumption 3.4)

Modulus of elasticity = 203 *GPa* (at 93 *°C*)
Modulus of elasticity = 196 *GPa* (at 204 *°C*)

SA-240 S31600 (316 SS) (Inner vessel and inner vessel lids):

Density = 7980 $kg/m^3$ (at RT) (Ref. 11, Table X1.1, p. 7)

Poisson's ratio = 0.298 (at RT) (Ref. 10, Figure 15, p. 755)

Modulus of elasticity = 186 $GPa$ ($27.0 \cdot 10^6$ $psi$) (at 300 $^oF = 149\ ^oC$) (Ref. 12, Sec. II, Part D, Subpart 2, Table TM-1)
Modulus of elasticity = 183 $GPa$ ($26.5 \cdot 10^6$ $psi$) (at 400 $^oF = 204\ ^oC$) (Ref. 12, Sec. II, Part D, Subpart 2, Table TM-1)

TSw2 Rock:

Density = 2370 $kg/m^3$ (at RT) (Assumption 3.6)

Poisson's ratio = 0.21 (at RT) (Assumption 3.5)

Modulus of elasticity = 33.0 $GPa$ (at RT) (Assumption 3.5)

### 5.1.1 Calculations for Elevated-Temperature Material Properties

The structural calculations are performed for material properties evaluated at 150 $^oC$ (see Assumptions 3.1 and 3.2). The material properties at this temperature are obtained by linear interpolation of corresponding material properties presented in Section 5.1 by using the formula:

$$p = p(T) = p_l + \left(\frac{T - T_l}{T_u - T_l}\right) \cdot (p_u - p_l)$$

Subscripts $u$ and $l$ denote the bounding values of generic material property $p$ at the corresponding bounding temperatures.

The following parameters are used in the subsequent calculations:

$s_y \approx \sigma_y$ = yield strength
$s_u$ = engineering ultimate strength
$el$ = elongation
$E$ = modulus of elasticity

These material properties are obtained from Section 5.1.

In the case of Alloy 22, the material properties at 150 $^oC$ are:

$$\sigma_y \approx s_y = 338 + [(150 - 93) \cdot (283 - 338)]/(204 - 93) = 310\ MPa$$
$$s_u = 738 + [(150 - 93) \cdot (676 - 738)]/(204 - 93) = 706\ MPa$$
$$el = 0.65 + [(150 - 93) \cdot (0.66 - 0.65)]/(204 - 93) = 0.66$$
$$E = 203 + [(150 - 93) \cdot (196 - 203)]/(204 - 93) = 199\ GPa$$

Similarly, for 316 SS at 150 $^{\circ}C$ :

$$E = 186 + [(150 - 149) \cdot (183 - 186)]/(204 - 149) = 186\,GPa$$

### 5.1.2 Calculations for True Measures of Ductility

The material properties in Section 5.1 refer to engineering stress and strain definitions: $s = P/A_0$ and $e = L/L_0 - 1$ (see Ref. 13, Chapter 9), where $P$ stands for the force applied during a static tensile test, $L$ is the length of the deformed specimen, and $L_0$ and $A_0$ are the original length and cross-sectional area of the specimen, respectively. The engineering stress-strain curve does not give a true indication of the deformation characteristics of a material during plastic deformation since it is based entirely on the original dimensions of the specimen. In addition, ductile metal that is pulled in tension becomes unstable and necks down during the course of the test. Hence, LS-DYNA V960.1106 FE code requires input in terms of true stress and strain definitions: $\sigma = P/A$ and $\varepsilon = \ln(L/L_0)$ (see Ref. 13, Chapter 9).

The relationships between the true stress and strain definitions and the engineering stress and strain definitions, $\sigma = s \cdot (1 + e)$ and $\varepsilon = \ln(1 + e)$, can be readily derived based on constancy of volume ($A_0 \cdot L_0 = A \cdot L$) and strain homogeneity during plastic deformation (see Ref. 13, Chapter 9). These expressions are applicable only in the hardening region of the stress-strain curve that is limited by the onset of necking.

The following parameters are added in the subsequent calculations:

$\sigma_u$ = true ultimate strength

$e_y \approx \varepsilon_y$ = strain corresponding to yield strength

$e_u$ = engineering uniform strain (engineering strain corresponding to ultimate strength)

$\varepsilon_u$ = true uniform strain (true strain corresponding to ultimate strength)

In absence of data on the uniform strain in available literature, the uniform strain needs to be estimated based on the character of stress-strain curves and elongation (strain corresponding to rupture of the tensile specimen). The stress-strain curves for Alloy 22 do not manifest three-stage (elastic-hardening-softening) deformation character (see Assumption 3.8). Therefore, the elongation reduced by 10 percent (to take into account the specimen-failure part of the stress-strain curve) is assumed for uniform strain.

Thus, the engineering uniform strain for Alloy 22 at at 150 $^{\circ}C$ is:

$$e_u = 0.9 \cdot el = 0.9 \cdot 0.66 = 0.59$$

The true measures of ductility at 150 $^{\circ}C$ are:

$$\varepsilon_u = \ln(1+e_u) = \ln(1+0.59) = 0.46$$
$$\sigma_u = s_u \cdot (1+e_u) = 706 \cdot (1+0.59) = 1120\ MPa$$

Therefore, the true ultimate strength of Alloy 22 at 150 $^{\circ}C$ is 1120 *MPa*.

### 5.1.3 Calculation for Tangent Modulus

As previously discussed, the results of this simulation are required to include elastic and plastic deformations for Alloy 22. When the materials are driven into the plastic range, the slope of the stress-strain curve continuously changes. A ductile failure is preceded by a protracted regime of hardening and substantial accumulation of inelastic strains. Thus, a simplification for the stress-strain curve is needed to incorporate plasticity into the FE analysis. An approximation commonly used in engineering is to use a straight line that connects the yield strength point and the ultimate strength point of the material (bilinear elastoplastic constitutive behavior). The tangent modulus ($E_1$) represents the slope of the stress-strain curve in the plastic region. In the case of Alloy 22, the tangent modulus at 150 $^{\circ}C$ is:

$E_1 = (\sigma_u - \sigma_y)/(\varepsilon_u - \sigma_y/E) = (1.12 - 0.310)/(0.46 - 0.310/199) = 1.77\ GPa$ (see Sections 5.1, 5.1.1, and 5.1.2)

## 5.2 FINITE ELEMENT REPRESENTATION

Three-dimensional FE representation, used for impact simulations, is presented in Figure 2. As seen in this figure, the FE representation consists of the WP, the pallet, and the invert surface. The FE representation is developed in ANSYS V5.6.2, by using the dimensions provided in References 22 (Sheet 2) and 24 and Attachments I and II (see also Assumptions 3.7, 3.10, 3.13, and 3.15).

Two different configurations are studied in this document.

In the first configuration (presented in Figure 3) the WP is horizontal (i.e., the centerline of the WP is parallel to the invert surface). The centerline of the WP is also parallel to the longitudinal symmetry plane of the pallet but it does not lie on that plane. Consequently, the WP simultaneously impacts the pallet on both axial ends but only on one side from the pallet symmetry plane (two-point impact). The first configuration will be referred to as the horizontal drop configuration henceforth.

The most notable difference in the second configuration (presented in Figures 2 and 4) is that the centerline of the WP is inclined 5 degrees with respect to the invert surface. The centerline of the WP is also inclined 1 degree with respect to the longitudinal symmetry plane of the pallet (see Figure 4a). Consequently, the WP impacts the pallet on one axial end and one side from the pallet symmetry plane (one-point impact). The second configuration will be referred to as the oblique drop configuration henceforth.

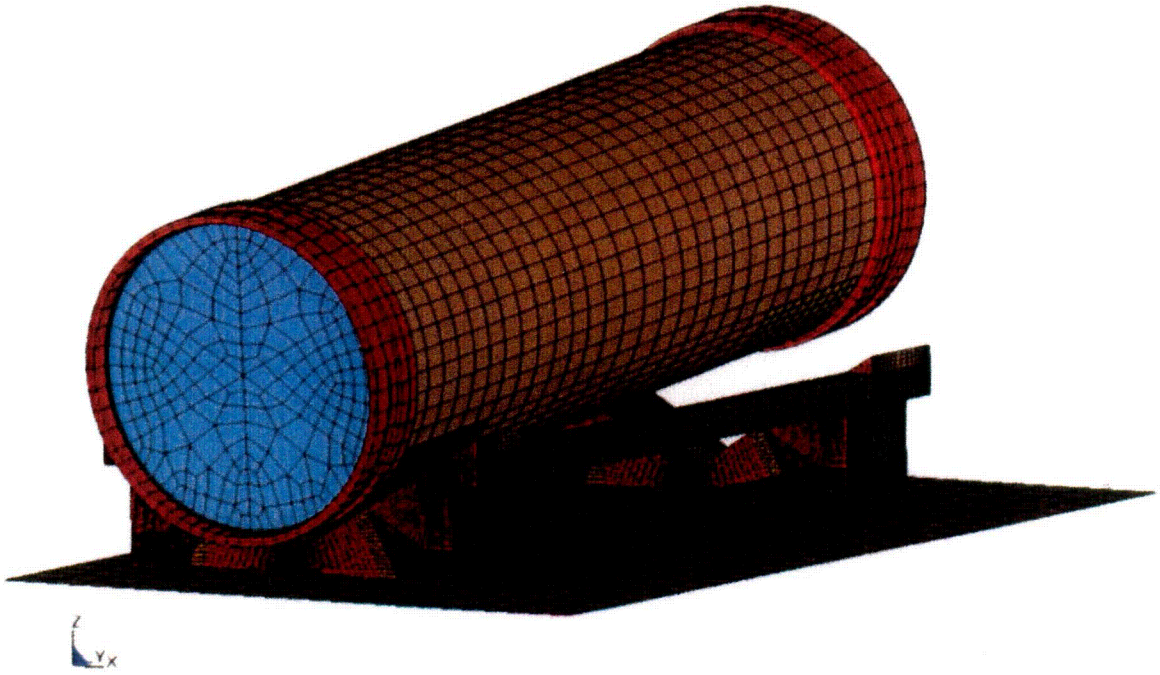

Figure 2. Simulation Setup

C01

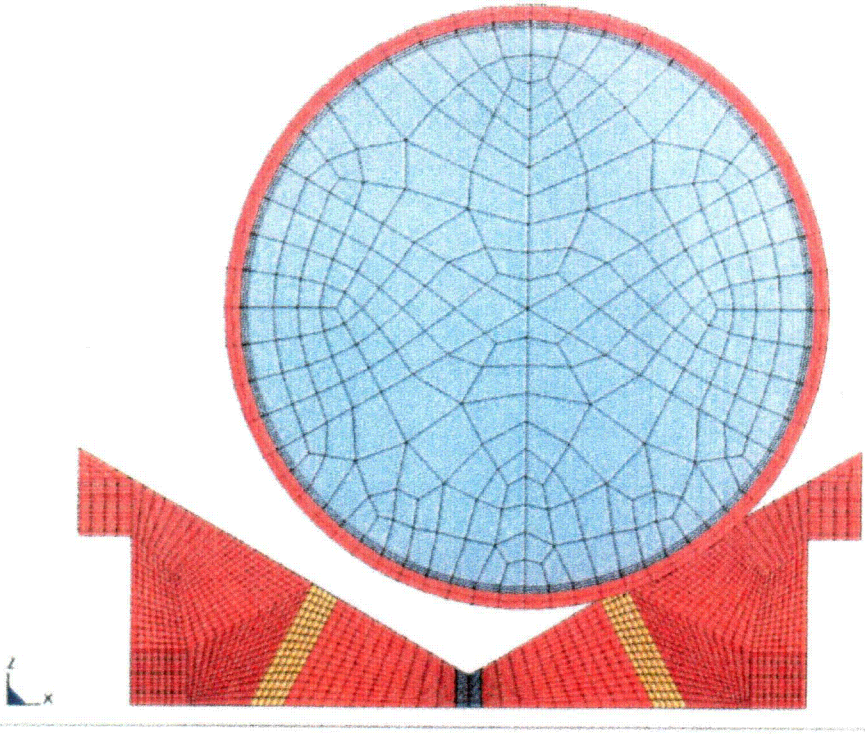


(a)

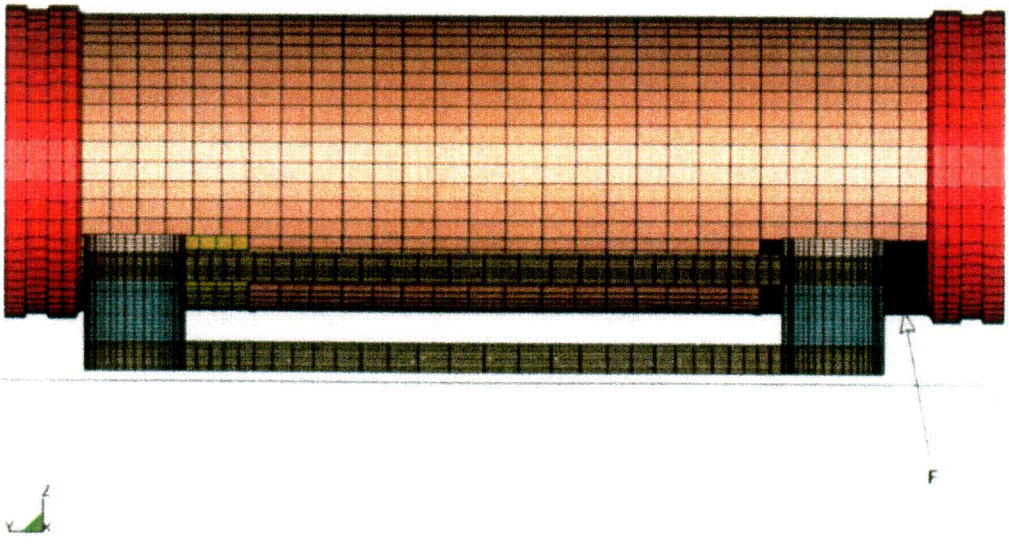


(b)

Figure 3. Horizontal Impact Configuration: (a) End View, and (b) Side View

C02

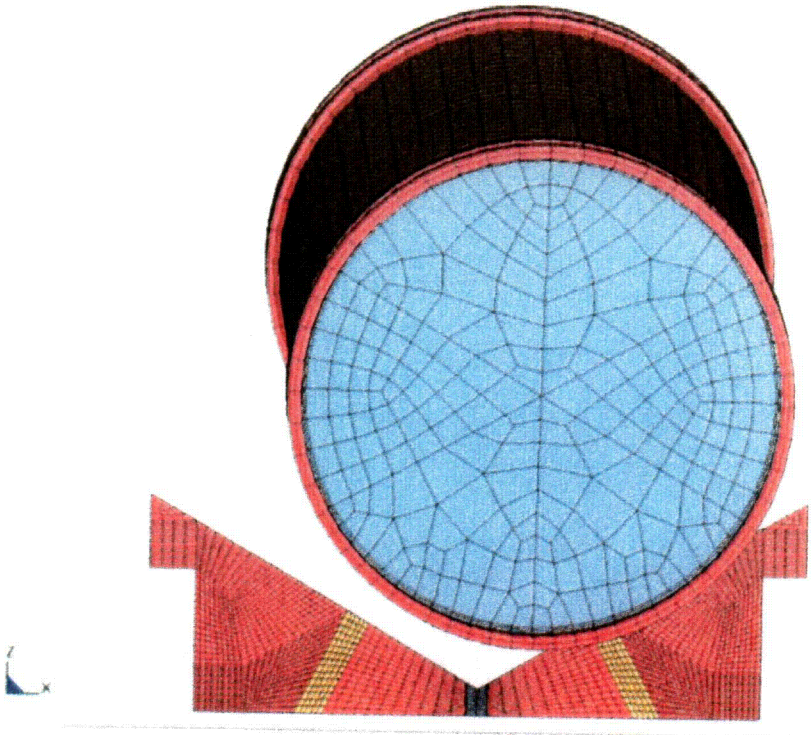

(a)

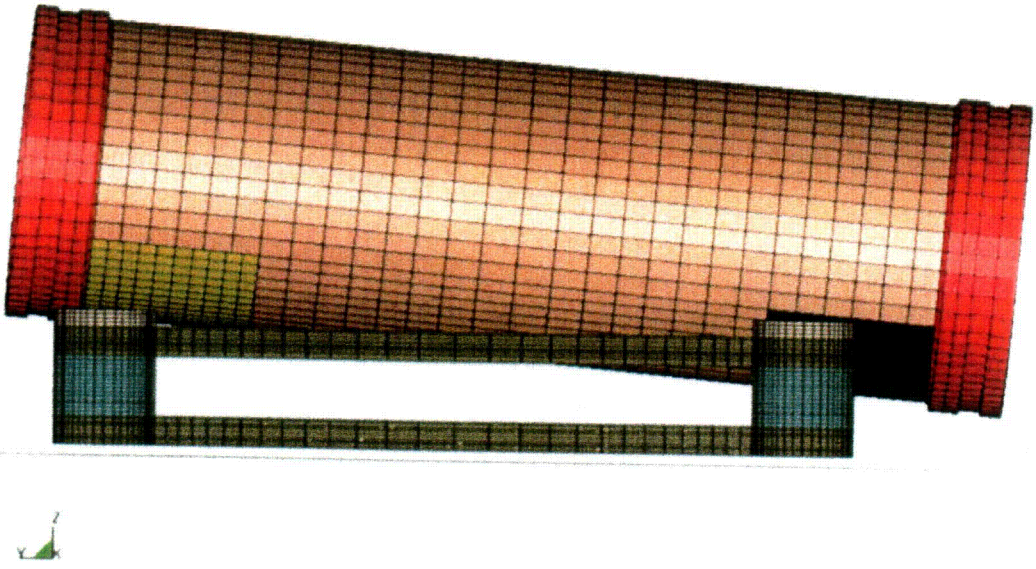

(b)

Figure 4. Oblique Impact Configuration: (a) End View, and (b) Side View

These two configurations are selected as typical examples of the impact configurations that can occur during an earthquake simulation. It is readily acknowledged that this selection does not imply that the two configurations yield the bounding set of results either in terms of maximum stress intensity or damaged area.

The WP is represented as symmetric in this study (Assumption 3.15); both WP ends are, in FE representation, based on the bottom-end configuration (see Attachment I and Reference 24). The details of the WP top end (such as, for example, the extended OCB lid and closure lid) are ignored and their mass is taken into account by increasing the thickness of the OCB lid.

For the drop simulation the thickness of the WP OCB is reduced by 2 *mm* (from 20 *mm* to 18 *mm*; see Assumption 3.10). This thickness reduction is used for seismic calculations (Ref. 16, Section 3), and is retained for consistency in the present FE mesh study. It needs to be emphasized, though, that the objective of this calculation is not to rigorously evaluate the OCB-thickness reduction due to corrosion or the corrosion-acceleration effects. A depth of corroded layer of 2 *mm* is, therefore, conservatism within the stated objective of this calculation (see Section 1).

The WP OCB, the trunnion sleeve, and the boundary walls are represented by eight-node solid (brick) elements. The part of the OCB that can come in contact with the pallet (see Figures 2 and 3) is of the most importance in this calculation. The FE representation of this region of the OCB is finely meshed on one side of the WP (F in Figure 3b), with four layers of brick elements across the OCB thickness (in-plane mesh density varies in different FE meshes [see Tables 1 and 2]). All results reported in this document are evaluated for the part of the OCB designated by F in Figure 3b. The WP OCB is represented as elastoplastic (the bilinear kinematic hardening) while the inner vessel and inner vessel lids are rigid. Two regions of the OCB that can get in contact with pallet are connected to the remaining part of the OCB by tied-interface contacts (Ref. 17, Section 23.9 and Ref. 18, p. 6.29). The effect of a potential shell-element representation of the OCB is studied in Attachment VI.

The WP inner vessel and its lids, the pallet, and the invert are represented by shell elements. Shell elements are adequate for representation of the pallet since their dominant mode of deformation is bending. Additionally, the stress state in the pallet is of secondary importance in this analysis that is focused on the WP OCB. In order to reduce the computer execution time while preserving all the features relevant for the solution, the inner vessel and inner vessel lid, as well as the invert surface, are represented as rigid bodies. Thus, the use of shell elements (as opposed to possible use of solid elements) for representation of these parts is inconsequential.

The structure of the 21-PWR WP is simplified by reducing the structure of the inner vessel and its interior structure, including the SNF, to a thick-wall cylinder of circular cross section and uniform density (Assumption 3.7). The outside diameter of the inner vessel is kept unchanged. The thickness of the inner vessel is determined by using density of 316 SS and matching the total mass of the inner vessel and internals as presented in Attachment I. The benefit of using this approach is to reduce the computer execution time while preserving all features of the problem relevant to the structural response.

The FE representation of the 21-PWR WP is developed in such a way that the loose-fit radial gap between the outer and inner vessel is maximized to 4 *mm* (Ref. 25, Section 8.1.8). Consequently, the inner vessel is free to move within the OCB.

Contacts are specified between the OCB and inner vessel, OCB and pallet, and pallet and invert. In absence of more specific data, the dynamic friction coefficients for all contacts are selected to be 0.55 (see Assumption 3.11). The functional friction coefficient used by LS-DYNA V960.1106 FE code is defined in terms of static and dynamic friction coefficients and relative velocity of the surfaces in contact (Ref. 18, p. 6.9). The effect of the relative velocity of the surfaces in contact is introduced by the way of a fitting parameter—exponential decay coefficient. The variation of friction coefficient between the static and dynamic value as a function of relative velocity of the surfaces in contact is not available in literature for the materials used in this calculation. Therefore, it is not possible to objectively evaluate the exponential decay coefficient. Hence, the effect of the relative velocity of the surfaces in contact is neglected in these calculations by assuming that the functional friction coefficient and the static friction coefficient are equal to the dynamic friction coefficient (Assumption 3.12). This approach maximizes the relative motion of the unanchored repository components by minimizing the friction coefficient within the given FE-analysis framework.

The WP OCB is in a stress-free condition prior to impact. The effect of residual stresses caused by solution annealing and double-sided quenching is studied in Attachment VII.

The FE representation is then used in LS-DYNA V960.1106 to perform a transient dynamic analysis of the WP impacting the pallet. To reduce the computer execution time, the WP is initially set in a position just before impact and initial velocity is assigned to all its nodes.

The stiffness-proportional damping is applied in the finely meshed OCB region (F in Figure 3b) for the entire duration of the simulation. The stiffness-proportional damping is an effective technique for reduction of the high-frequency noise, and it does not affect the rigid body motion. The necessity for damping and the choice of the damping coefficient are discussed in detail in Attachment III. In addition to the stiffness-proportional damping being applied locally (in the finely meshed OCB region), the system damping is also applied but globally (to all objects) and only after the WP bounces off the pallet. The purpose of the global system damping is to reduce the time necessary to obtain steady-state results (i.e., residual stresses) as much as possible (see Section 5.2.1 for details).

Results obtained for four FE meshes for the horizontal drops and five FE meshes for the oblique drops are presented in this document. The typical element size of the coarsest FE mesh (designated henceforth as "Mesh 1") corresponds to the one used in Reference 16 (Section 5.2). The subsequent FE representations (named: "Mesh 2", "Mesh 3", "Mesh 4", and, in the case of oblique drop, "Mesh 5") are obtained by substantially refining the in-plane discretization of the part of the OCB that can contact the pallet (part F in Figure 3b). Specifically, the typical element size in the Mesh 2, Mesh 3, Mesh 4, and Mesh 5 (when applicable) is respectively 9, 16, 25, and 36 times smaller than the one in the Mesh 1 (see Tables 1 and 2).

Table 1. Parameters of Typical Element for Horizontal Drop

| Typical Element | Mesh 1 | Mesh 2 | Mesh 3 | Mesh 4 |
|---|---|---|---|---|
| Number | 45015 | 46983 | 48675 | 50967 |
| Dimensions (*mm*) | 22.2×34.0 | 7.38×11.3 | 5.54×8.51 | 4.43×6.81 |
| Area ($mm^2$) | 755 | 83.4 | 47.1 | 30.2 |

Table 2. Parameters of Typical Element for Oblique Drop

| Typical Element | Mesh 1 | Mesh 2 | Mesh 3 | Mesh 4 | Mesh 5 |
|---|---|---|---|---|---|
| Number | 45783 | 51877 | 58943 | 67040 | 76535 |
| Dimensions (*mm*) | 21.4×34.0 | 7.13×11.3 | 5.35×8.51 | 4.28×6.81 | 3.22×5.67 |
| Area ($mm^2$) | 728 | 80.6 | 45.5 | 29.1 | 18.3 |

### 5.2.1 System Damping

In order to obtain steady-state results (i.e., residual stresses) in a reasonable time, it is necessary to apply system damping after the WP bounces off the pallet. The system damping is applied globally.

As discussed in Reference 17 (Section 28.2), the most appropriate damping constant for the system is usually the critical damping constant. According to the calculation presented in Reference 16 (Section 5.2.2), the critical damping coefficient is approximately $700\,rad/s$. Nonetheless, in order to avoid over-damping of the system the damping constant is conservatively reduced to $DC = 200\,rad/s$ (the same reduction is applied in Reference 16 as well). Furthermore, the parametric study of various damping constants for the FE representation of the 21-PWR WP, presented in Reference 27, confirms the appropriateness of this choice. According to Figure 4 presented in Reference 27 (Section 5.3.4), the system is obviously not over-damped for $DC = 200\,rad/s$, and the steady-state results are reached in reasonable time.

# 6. RESULTS

Attachment VIII includes the input files and results files that show execution of the programs occurred correctly. The stress and strain time histories, residual stress distribution plots, and damaged areas have been obtained by interactively using the postprocessor LSPOST V2.

Tables 3 and 4 present the average CPU time necessary for execution of horizontal and oblique drop calculations, respectively. The CPU time is, for the sake of convenience, presented in CPU days necessary for simulation of 1 second of the event. The purpose of this presentation is to illustrate the increase of the computational workload with the mesh refinement.

Table 3. Average CPU Time for Execution of Horizontal-Drop Calculation

| Impact Speed (m/s) | CPU Time (CPU days per second of physical time) | | | |
|---|---|---|---|---|
| | Mesh 1 | Mesh 2 | Mesh 3 | Mesh 4 |
| 1 | 10.2 | 19.3 | 27.5 | 46.9 |
| 3 | 10.4 | 19.1 | 26.7 | 46.1 |
| 5 | 10.3 | 19.8 | 28.2 | 46.9 |
| 8 | 10.6 | 20.5 | 30.0 | 47.5 |

Table 4. Average CPU Time for Execution of Oblique-Drop Calculation

| Impact Speed (m/s) | CPU Time (CPU days per second of physical time) | | | | |
|---|---|---|---|---|---|
| | Mesh 1 | Mesh 2 | Mesh 3 | Mesh 4 | Mesh 5 |
| 1 | 10.0 | 15.9 | 22.1 | 31.3 | 62.2 |
| 3 | 10.0 | 16.3 | 22.7 | 33.3 | 65.5 |
| 5 | 10.2 | 16.7 | 23.4 | 32.6 | 63.2 |
| 8 | 10.2 | 16.3 | 23.6 | 32.5 | 63.4 |

## 6.1 DAMAGED AREA

Recall that the area of the WP OCB where the residual 1$^{st}$ principal stress exceeds certain limits is called "damaged area" throughout this document (with exception of Attachment V; see Section 1).

The damaged areas for the different meshes (discussed in Section 5.2) and four different impact speeds are presented for the horizontal and oblique drops in Tables 5 and 6, respectively.

Table 5. Damaged Area for Horizontal Drop

| Impact Speed (m/s) | Damaged Area ($\times 10^{-3}$ $m^2$) (80% criterion / 90% criterion) | | | |
|---|---|---|---|---|
| | Mesh 1 | Mesh 2 | Mesh 3 | Mesh 4 |
| 1 | 3.69 / 0.75 | 0.08 / 0 | 0.57 / 0.09 | 0.51 / 0.09 |
| 3 | 0.73 / 0 | 2.32 / 0.33 | 1.34 / 0.18 | 1.37 / 0.63 |
| 5 | 0.72 / 0 | 0.59 / 0.08 | 0.42 / 0.14 | 0.48 / 0.06 |
| 8 | 11.16 / 2.99 | 7.47 / 2.46 | 7.61 / 1.98 | 8.72 / 1.72 |

Table 6. Damaged Area for Oblique Drop

| Impact Speed (m/s) | Damaged Area ($\times 10^{-3}\ m^2$) (80% criterion / 90% criterion) | | | | |
|---|---|---|---|---|---|
| | Mesh 1 | Mesh 2 | Mesh 3 | Mesh 4 | Mesh 5 |
| 1 | 4.36 / 0.73 | 4.12 / 1.05 | 3.32 / 0.86 | 4.46 / 1.80 | 4.17 / 1.35 |
| 3 | 7.27 / 0.73 | 1.46 / 0 | 1.87 / 0.36 | 1.61 / 0.21 | 1.25 / 0.09 |
| 5 | 6.56 / 0 | 1.13 / 0.56 | 0.18 / 0 | 1.73 / 0.49 | 0.64 / 0 |
| 8 | 3.63 / 0.73 | 3.97 / 0.97 | 1.09 / 0.09 | 1.46 / 0.24 | 2.48 / 0.22 |

The first observation that can be made based on the results presented in Tables 5 and 6 is that, with exception of the horizontal drop with 3 $m/s$, the use of Mesh 1 always results in a conservative estimate of the damaged area.

Second, it seems that the results are not asymptotically approaching the "correct" value with the mesh refinement but are rather approaching it in an oscillatory fashion (with a perpetually diminishing error). This conclusion is somewhat speculative since it is difficult to make a judgement on the (oscillatory) character of a curve based on 4 or 5 points.

Finally, it is necessary to discuss the change of the damaged area with the increase of impact speed. It is not intuitively clear why the maximum damaged area should be encountered at the smallest impact speed in the case of oblique drops regardless of the FE mesh size. Assuming that the results obtained by using the Mesh 4 for the horizontal drop are the most accurate, it can also be observed (Table 5) that the damaged area from the 1-*m/s* drop is larger than the one from the 5-m/s drop. (Note that the main difference between the horizontal drops and the oblique drops is that in the latter the contact region is more localized [see Figures 3 and 4].) The fine FE mesh (e.g., Mesh 5) is inherently better suited to capture the localized deformation of the OCB (i.e., dent in the OCB) than the coarse FE mesh (e.g., Mesh 1) as it can be seen from Figure 5.[1] Thus, unlike the fine mesh, the damage in the impact region of the coarse mesh is smeared over the larger OCB region (see Figure 6).

The residual 1st principal stress distribution in the OCB is presented in Figure 7 for two oblique drops (with Mesh 5) with 1 *m/s* and 8 *m/s*. It is obvious that the size of the dent is much larger for the larger impact speed. Nonetheless, the damaged area in the case of an 8-m/s drop is also more localized around the dent.

In summary, it appears, according to the presented results, that it is essential to properly capture the localized deformation (i.e., dent) in order to avoid the overestimation of damaged area. The more localized the loading (and consequently the deformation), the more stringent the meshing

[1] The stress fringe levels on all residual 1st principal stress plots throughout this document are presented in Pascals ( $Pa = N/m^2$ ). The number of stress fringe levels is reduced to three to emphasize the amount and distribution of damage. All elements with residual 1st principal stress below 248 *MPa* are blue. All elements with residual 1st principal stress from 248 *MPa* to 279 *MPa* are green. Finally, all elements with residual 1st principal stress exceeding 279 *MPa* are red.

requirements. (Note that convergence of the damaged area is faster for the less-localized horizontal drop than for the oblique drop.)

## 6.2 MAXIMUM STRESS INTENSITY

The stress intensity presented in this section is defined as:

$$\sigma_{ij} = \sigma_1 - \sigma_3 = 2 \cdot \tau_{max}$$

where $\sigma_1$ and $\sigma_3$ are maximum principal stress and minimum principal stress, respectively, and $\tau_{max}$ is the maximum shear stress (Ref. 12, Section III, Division 1, NB-3213.1; and Ref. 13, Chapter 3).

The maximum stress intensity for the different meshes and four different impact speeds are presented for the horizontal and oblique drops in Tables 7 and 8, respectively.

Table 7. Maximum Stress Intensity for Horizontal Drop

| Impact Speed (m/s) | Maximum Stress Intensity (MPa) | | | |
|---|---|---|---|---|
| | Mesh 1 | Mesh 2 | Mesh 3 | Mesh 4 |
| 1 | 361 | 395 | 409 | 419 |
| 3 | 370 | 453 | 483 | 518 |
| 5 | 384 | 576 | 631 | 680 |
| 8 | 391 | 630 | 680 | 761 |

Table 8. Maximum Stress Intensity for Oblique Drop

| Impact Speed (m/s) | Maximum Stress Intensity (MPa) | | | | |
|---|---|---|---|---|---|
| | Mesh 1 | Mesh 2 | Mesh 3 | Mesh 4 | Mesh 5 |
| 1 | 368 | 446 | 456 | 485 | 528 |
| 3 | 393 | 544 | 590 | 631 | 656 |
| 5 | 396 | 638 | 742 | 800 | 877 |
| 8 | 387 | 691 | 791 | 837 | 946 |

The first observation that can be made based on the results presented in Tables 7 and 8 is that the Mesh 1 is too coarse to capture the maximum stress intensity. This is not surprising keeping in mind the large aspect ratio of the typical element in Mesh 1 (see, for example, Figure 5a). This inadequacy becomes more pronounced as the impact speed increases.

It is difficult, based on the presented results, to identify a FE mesh that provides completely satisfactory stress-intensity results with regards to mesh objectivity. It is obvious that increase of the impact speed imposes harsher meshing requirements. It is not obvious though that the mesh refinement from Mesh 4 to Mesh 5 is productive, since it does not improve the aspect ratio of a typical element. Further mesh refinement in both in-plane directions with four elements across OCB thickness would adversely affect the element aspect ratio. On the other hand, mesh refinement in the

hoop direction only (see Tables 1 and 2) would improve the aspect ratio of typical element, which could have a beneficial effect on the results. Finally, the mesh refinement in all three directions would further increase already tremendous computational requirements (see Tables 3 and 4).

The accuracy and representativeness of the results of this calculation are deemed acceptable. The output values are reasonable for the given inputs. The results are suitable for the intended use. The uncertainties are taken into account by varying the damage threshold and by using the typical mechanical properties for the OCB material (Alloy 22).

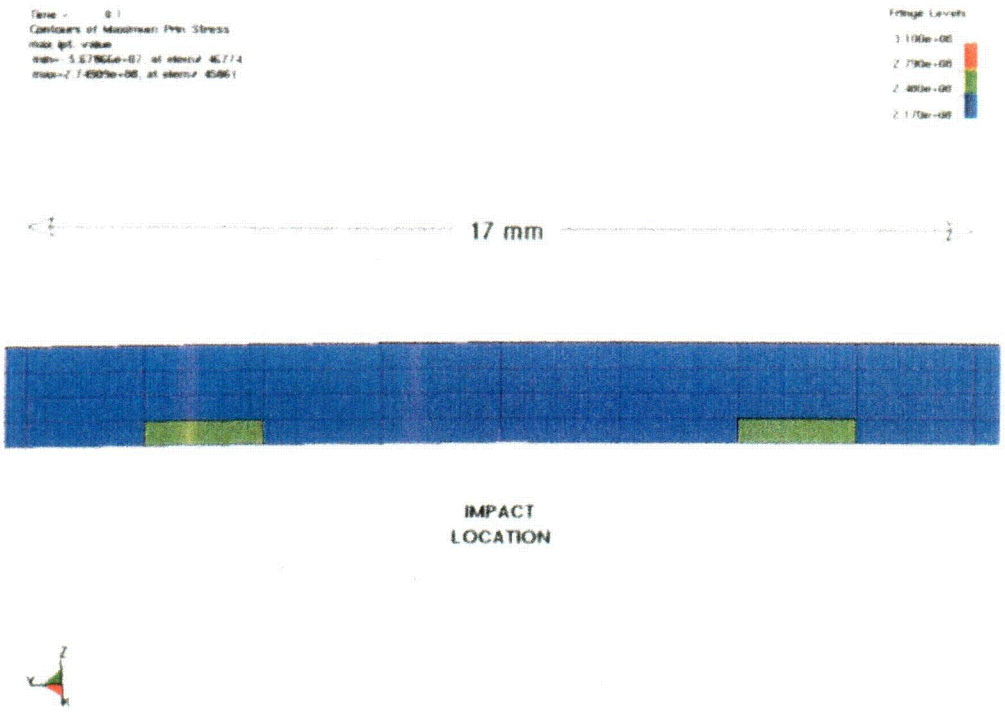


(a)

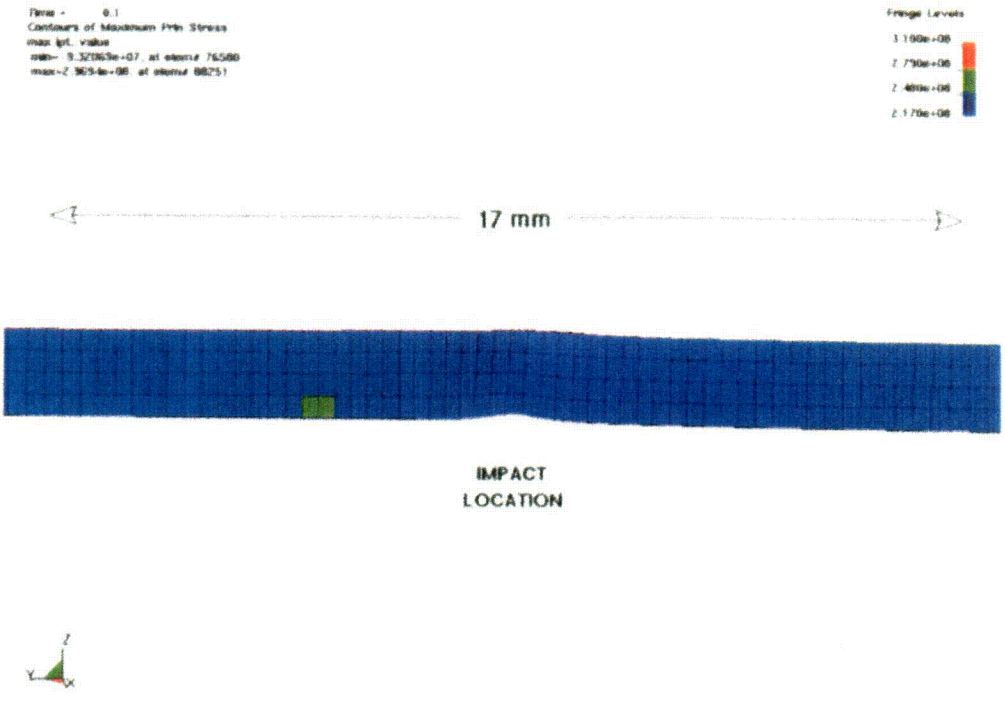


(b)

Figure 5. Through-Wall Deformation and Accompanying Residual 1st Principal Stress Distribution for 5-*m/s* Oblique Drop: (a) Mesh 1, and (b) Mesh 5

C04

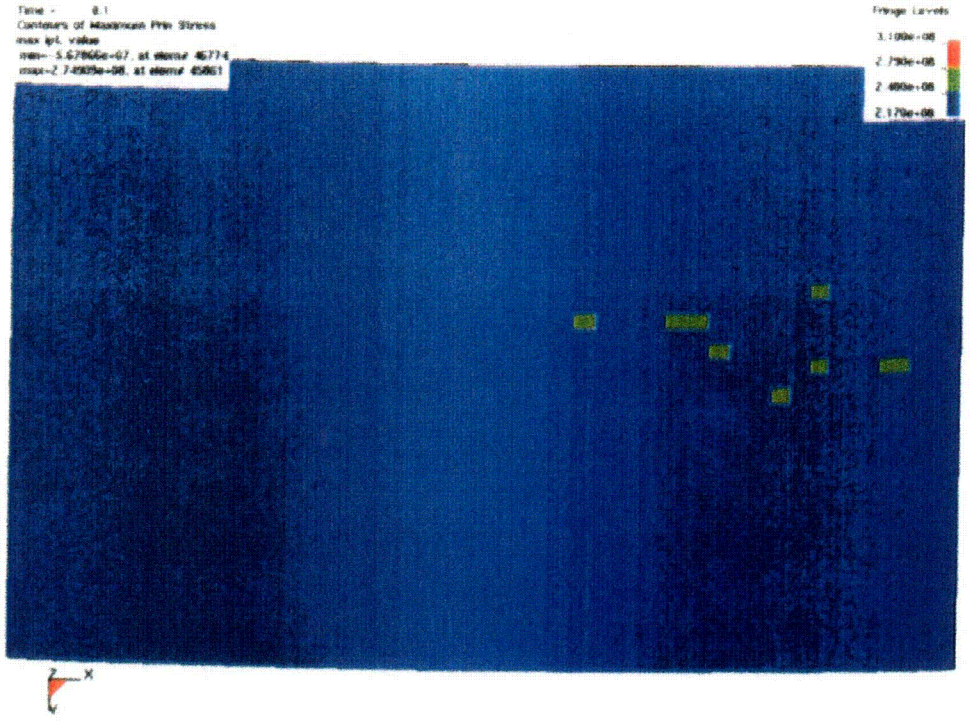

(a)

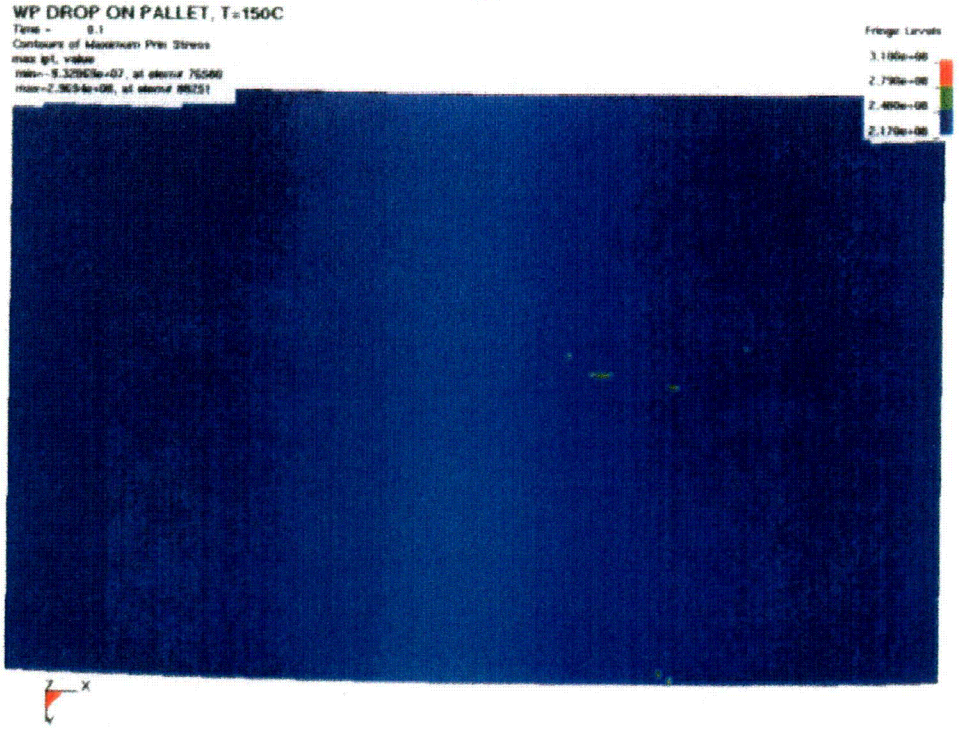


(b)

Figure 6. Residual 1st Principal Stress Distribution for 5-*m/s* Oblique Drop (Bottom View): (a) Mesh1, and (b) Mesh 5

C05

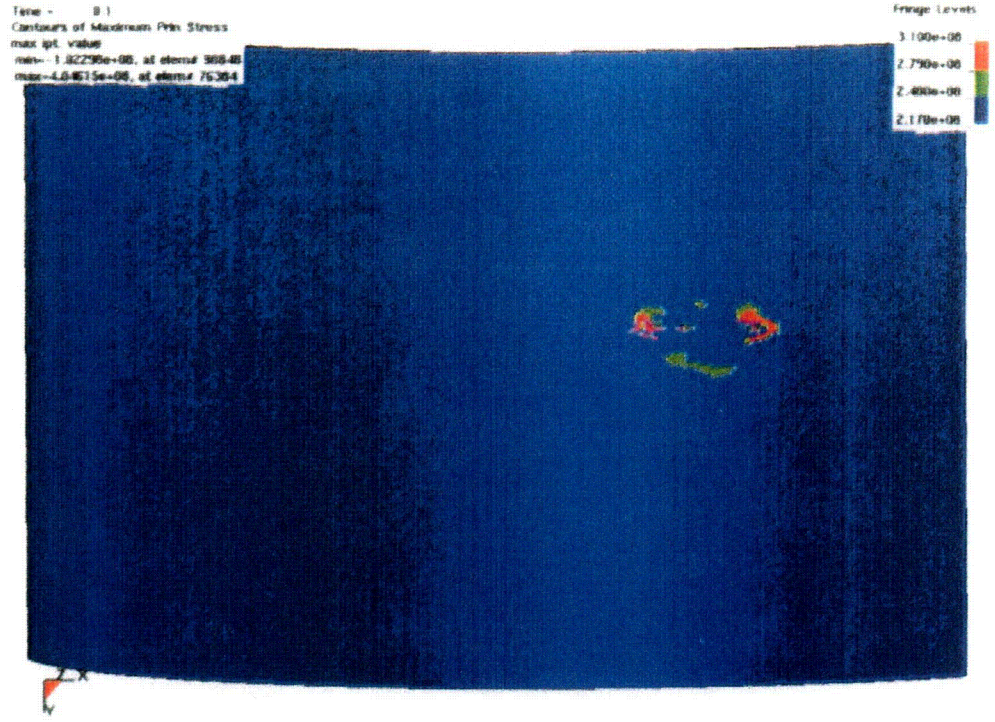


(a)

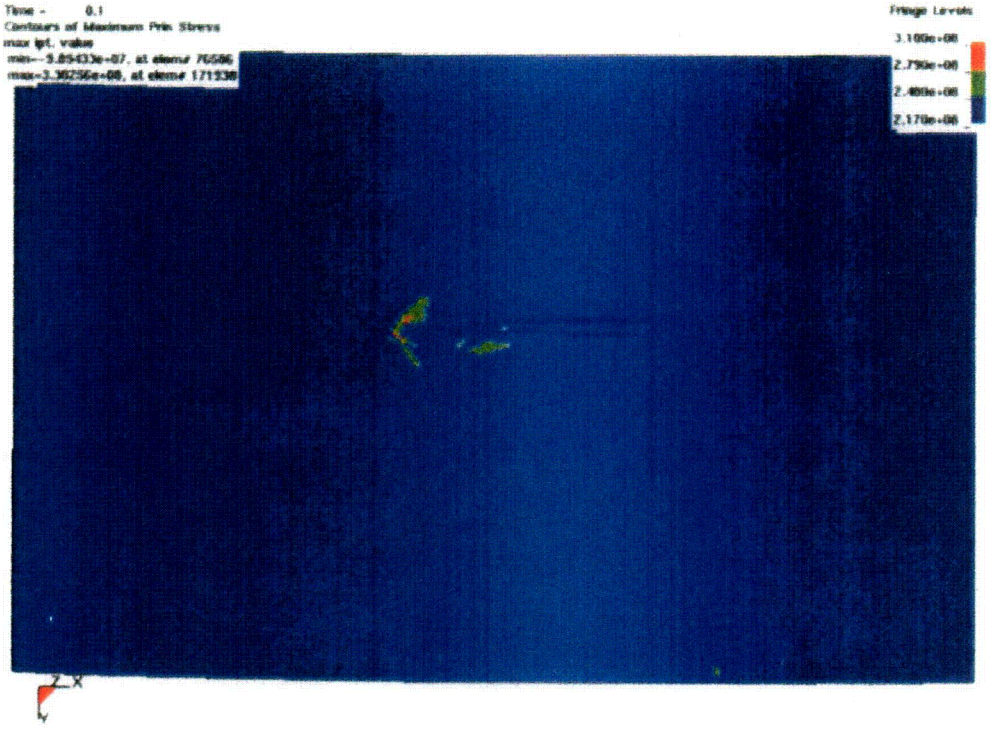


(b)

Figure 7. Residual 1st Principal Stress Distribution for Oblique Drop (Bottom View, Mesh 5) for Impact Speed: (a) 1 *m/s*, and (b) 8 *m/s*

C06

## 7. REFERENCES

1. AP-3.12Q, Rev. 2, ICN 1. *Design Calculations and Analyses.* Washington, D.C.: U.S. Department of Energy, Office of Civilian Radioactive Waste Management. ACC: DOC.20030827.0013.

2. AP-SI.1Q, Rev. 5, ICN 2. *Software Management.* Washington, D.C.: U.S. Department of Energy, Office of Civilian Radioactive Waste Management. ACC: DOC.20030902.0003.

3. MO0308CPRSPMWP.000. Calculation Package for Residual Stress Analyses on the 21 PWR Mockup Waste Package Outer Shell Due to Quenching and General Corrosion Using a Side-wall Thickness of 20 mm, TRW-06Q-319 (C). Submittal date: 08/20/2003.

4. DOE (U.S. Department of Energy) 2003. *Quality Assurance Requirements and Description.* DOE/RW-0333P, Rev. 13. Washington, D.C.: U.S. Department of Energy, Office of Civilian Radioactive Waste Management. ACC: DOC.20030422.0003.

5. CRWMS M&O 1999. *Classification of the MGR Uncanistered Spent Nuclear Fuel Disposal Container System.* ANL-UDC-SE-000001 REV 00. Las Vegas, Nevada: CRWMS M&O. ACC: MOL.19990928.0216.

6. BSC (Bechtel SAIC Company) 2002. *Software Code: ANSYS.* V5.6.2. HP-UX 11.00. 10364-5.6.2-01.

7. BSC (Bechtel SAIC Company) 2002. *Software Code: LS-DYNA.* V960.1106. HP9000. 10300-960.1106-00.

8. McKenzie, D.G., IV. 2002. *Waste Package Design Methodology Report.* TDR-MGR-MD-000006 REV 02. Las Vegas, Nevada: Bechtel SAIC Company. ACC: MOL.20020404.0085.

9. MO0003RIB00071.000. Physical and Chemical Characteristics of Alloy 22. Submittal date: 03/13/2000.

10. ASM (American Society for Metals) 1980. *Properties and Selection: Stainless Steels, Tool Materials and Special-Purpose Metals.* Volume 3 of *Metals Handbook.* 9th Edition. Benjamin, D., ed. Metals Park, Ohio: American Society for Metals. TIC: 209801.

11. ASTM G 1-90 (Reapproved 1999). 1999. *Standard Practice for Preparing, Cleaning, and Evaluating Corrosion Test Specimens.* West Conshohocken, Pennsylvania: American Society for Testing and Materials. TIC: 238771.

12. ASME (American Society of Mechanical Engineers) 2001. *2001 ASME Boiler and Pressure Vessel Code (includes 2002 addenda).* New York, New York: American Society of Mechanical Engineers. TIC: 251425.

13. Dieter, G.E. 1976. *Mechanical Metallurgy.* 2nd Edition. Materials Science and Engineering Series. New York, New York: McGraw-Hill Book Company. TIC: 247879.

14. Nicholas, T. 1980. *Dynamic Tensile Testing of Structural Materials Using A Split Hopkinson Bar Apparatus.* AFWAL-TR-80-4053. Wright-Patterson Air Force Base, Ohio: Air Force Wright Aeronautical Laboratories. TIC: 249469.

15. LL020603612251.015. Slow Strain Rate Test Generated Stress Corrosion Cracking Data. Submittal date: 08/27/2002.

16. BSC (Bechtel SAIC Company) 2003. *Structural Calculations of Waste Package Exposed to Vibratory Ground Motion.* 000-00C-EBS0-00300-000-00B. Las Vegas, Nevada: Bechtel SAIC Company. ACC: ENG.20030520.0003.

17. Hallquist, J.O. 1998. *LS-DYNA, Theoretical Manual.* Livermore, California: Livermore Software Technology Corporation. TIC: 238997.

18. Livermore Software Technology Corporation. 2001. *LS-DYNA Keyword User's Manual.* Version 960. Two volumes. Livermore, California: Livermore Software Technology Corporation. TIC: 252119.

19. CRWMS M&O 1997. *Waste Container Cavity Size Determination.* BBAA00000-01717-0200-00026 REV 00. Las Vegas, Nevada: CRWMS M&O. ACC: MOL.19980106.0061.

20. Hill, R. 1998. *The Mathematical Theory of Plasticity.* New York, New York: Oxford University Press. TIC: 240262.

21. BSC (Bechtel SAIC Company) 2001. *Repository Multiple Waste Package Thermal Calculation.* CAL-WIS-TH-000010 REV 00. Las Vegas, Nevada: Bechtel SAIC Company. ACC: MOL.20010814.0330.

22. BSC (Bechtel SAIC Company) 2003. *Emplacement Pallet.* 000-MW0-TEP0-00101-000-00A, and -00102-000-00A. 2 Sheets. Las Vegas, Nevada: Bechtel SAIC Company. ACC: ENG.20030205.0007; ENG.20030205.0008.

23. MO9808RIB00041.000. Reference Information Base Data Item: Rock Geomechanical Properties. Submittal date: 08/05/1998.

24. BSC (Bechtel SAIC Company) 2001. *Repository Design, Waste Package, Project 21-PWR Waste Package with Absorber Plates, Sheet 1 of 3, Sheet 2 of 3, and Sheet 3 of 3.* DWG-UDC-ME-000001 REV A. Las Vegas, Nevada: Bechtel SAIC Company. ACC: MOL.20020102.0174.

25. Plinski, M.J. 2001. *Waste Package Operations Fabrication Process Report.* TDR-EBS-ND-000003 REV 02. Las Vegas, Nevada: Bechtel SAIC Company. ACC: MOL.20011003.0025.

26. Avallone, E.A. and Baumeister, T., III, eds. 1987. *Marks' Standard Handbook for Mechanical Engineers.* 9th Edition. New York, New York: McGraw-Hill. TIC: 206891.

27. BSC (Bechtel SAIC Company) 2003. *21-PWR Waste Package Side and End Impacts.* 000-00C-DSU0-01000-000-00B. Las Vegas, Nevada: Bechtel SAIC Company. ACC: ENG.20030227.0067.

28. MO0003RIB00079.000. Rock Mechanical Properties. Submittal date: 03/30/2000.

29. MO0303SPARESST.000. Residual Stress Failure Criteria for Seismic Damage Models of the Drip Shield and Waste Package. Submittal date: 03/04/2003.

## 8. ATTACHMENTS

Attachment I (2 pages): Design sketch (*21-PWR Waste Package Configurations for Site Recommendation* [SK-0175 REV 02, 2 sheets]) (Includes Reference 19)

Attachment II (13 pages): Design sketch (*Emplacement Pallet Long* [SK-0232 REV 00, 13 sheets])

Attachment III (5 pages): Damping of High-Frequency Oscillations

Attachment IV (2 pages): Effective Plastic Strain

Attachment V (1 page): Damaged Area Based on Stress Intensity

Attachment VI (3 pages): Shell-Element FE Representation

Attachment VII (4 pages): Effect of Residual Stress Caused by Annealing and Quenching

Attachment VIII (4 Compact Discs):
ANSYS V5.6.2 and LS-DYNA V960.1106 electronic files

Table 9 provides a list of files submitted on compact discs as Attachment VIII. The input and output ANSYS V5.6.2 and LS-DYNA V960.1106 files are archived by using WinZip V8.1. As identified in Section 4, WinZip V8.1 belongs to the category of automated office support systems that is exempt from the requirements defined in Reference 2 (see Section 2.1.1).

Table 9. List of Electronic Files in Attachment VIII

| Directory | | | File Name | Size (byte) | Time | Date |
|---|---|---|---|---|---|---|
| Compact Disc #1 | | | | | | |
| \Horizontal | \Mesh1 | \FER | FER.zip | 1,243,075 | 09:18 a.m. | 06 Aug 2003 |
| | | \vel1 | vel1.zip | 15,165,646 | 09:19 a.m. | 06 Aug 2003 |
| | | \vel3 | vel3.zip | 15,315,874 | 09:25 a.m. | 06 Aug 2003 |
| | | \vel5 | vel5.zip | 15,375,688 | 09:26 a.m. | 06 Aug 2003 |
| | | \vel8 | vel8.zip | 15,462,079 | 09:26 a.m. | 06 Aug 2003 |
| | \Mesh2 | \FER | FER.zip | 3,170,753 | 09:59 a.m. | 06 Aug 2003 |
| | | \vel1 | vel1.zip | 28,766,110 | 09:59 a.m. | 06 Aug 2003 |
| | | \vel3 | vel3.zip | 28,939,851 | 10:00 a.m. | 06 Aug 2003 |
| | | \vel5 | vel5.zip | 29,085,295 | 10:01 a.m. | 06 Aug 2003 |
| | | \vel8 | vel8.zip | 29,262,154 | 10:02 a.m. | 06 Aug 2003 |
| | \Mesh3 | \FER | FER.zip | 4,799,140 | 10:04 a.m. | 06 Aug 2003 |
| | | \vel1 | vel1.zip | 40,398,540 | 10:05 a.m. | 06 Aug 2003 |
| | | \vel3 | vel3.zip | 40,628,887 | 10:06 a.m. | 06 Aug 2003 |
| | | \vel5 | vel5.zip | 40,856,351 | 10:07 a.m. | 06 Aug 2003 |
| | | \vel8 | vel8.zip | 41,097,181 | 10:08 a.m. | 06 Aug 2003 |
| | \Mesh4 | \FER | FER.zip | 6,711,980 | 09:46 a.m. | 06 Aug 2003 |
| | | \vel1 | vel1.zip | 65,335,287 | 09:51 a.m. | 06 Aug 2003 |
| | | \vel3 | vel3.zip | 73,846,795 | 09:53 a.m. | 06 Aug 2003 |

| | | | | | | |
|---|---|---|---|---|---|---|
| | | \vel5 | vel5.zip | 68,584,064 | 07:06 a.m. | 11 Aug 2003 |
| | | \vel8 | vel8.zip | 70,406,498 | 09:56 a.m. | 06 Aug 2003 |
| Compact Disc #2 | | | | | | |
| \Oblique | \Mesh1 | \FER | FER.zip | 1,317,861 | 12:43 p.m. | 06 Aug 2003 |
| | | \vel1 | vel1.zip | 15,339,365 | 12:44 p.m. | 06 Aug 2003 |
| | | \vel3 | vel3.zip | 15,400,763 | 12:45 p.m. | 06 Aug 2003 |
| | | \vel5 | vel5.zip | 15,461,115 | 12:45 p.m. | 06 Aug 2003 |
| | | \vel8 | vel8.zip | 15,789,074 | 12:46 p.m. | 06 Aug 2003 |
| | \Mesh2 | \FER | FER.zip | 2,968,790 | 12:47 p.m. | 06 Aug 2003 |
| | | \vel1 | vel1.zip | 26,357,346 | 12:48 p.m. | 06 Aug 2003 |
| | | \vel3 | vel3.zip | 26,450,749 | 12:49 p.m. | 06 Aug 2003 |
| | | \vel5 | vel5.zip | 26,514,521 | 12:49 p.m. | 06 Aug 2003 |
| | | \vel8 | vel8.zip | 26,794,508 | 12:50 p.m. | 06 Aug 2003 |
| | \Mesh3 | \FER | FER.zip | 4,663,766 | 12:51 p.m. | 06 Aug 2003 |
| | | \vel1 | vel1.zip | 37,838,927 | 12:52 p.m. | 06 Aug 2003 |
| | | \vel3 | vel3.zip | 37,935,270 | 12:53 p.m. | 06 Aug 2003 |
| | | \vel5 | vel5.zip | 38,015,300 | 12:54 p.m. | 06 Aug 2003 |
| | | \vel8 | vel8.zip | 38,315,153 | 12:55 p.m. | 06 Aug 2003 |
| | \Mesh4 | \FER | FER.zip | 6,564,291 | 01:03 p.m. | 06 Aug 2003 |
| | | \vel1 | vel1.zip | 51,491,376 | 01:04 p.m. | 06 Aug 2003 |
| | | \vel3 | vel3.zip | 51,604,321 | 01:05 p.m. | 06 Aug 2003 |
| | | \vel5 | vel5.zip | 51,701,847 | 01:07 p.m. | 06 Aug 2003 |
| | | \vel8 | vel8.zip | 52,001,265 | 01:09 p.m. | 06 Aug 2003 |
| Compact Disc #3 | | | | | | |
| \Oblique | \Mesh5 | \FER | FER.zip | 8,822,392 | 01:14 p.m. | 06 Aug 2003 |
| | | \vel1 | vel1.zip | 76,035,935 | 01:15 p.m. | 06 Aug 2003 |
| | | \vel3 | vel3.zip | 76,164,201 | 01:17 p.m. | 06 Aug 2003 |
| | | \vel5 | vel5.zip | 76,282,941 | 01:19 p.m. | 06 Aug 2003 |
| | | \vel8 | vel8.zip | 76,553,819 | 01:20 p.m. | 06 Aug 2003 |
| \Residual | | \FER | FER.zip | 3,170,753 | 01:24 p.m. | 06 Aug 2003 |
| | | \Full | full.zip | 4,222,412 | 01:25 p.m. | 06 Aug 2003 |
| | | \Half | half.zip | 4,232,304 | 01:25 p.m. | 06 Aug 2003 |
| \Shell FER | | \Mesh3 | Mesh3.zip | 30,217,490 | 01:28 p.m. | 06 Aug 2003 |
| | | \Mesh4 | Mesh4.zip | 46,662,489 | 01:29 p.m. | 06 Aug 2003 |
| | | \Mesh5 | Mesh5.zip | 72,003,146 | 01:31 p.m. | 06 Aug 2003 |
| Compact Disc #4 | | | | | | |
| \Damping | | \COEF=1e-2 | COEF=1e-2.zip | 9,173,065 | 01:35 p.m. | 06 Aug 2003 |
| | | \COEF=1e-4 | COEF=1e-4.zip | 77,574,446 | 01:37 p.m. | 06 Aug 2003 |
| | | \COEF=1e-5 \VDC=0 \TStep=1e-3 | TStep=1e-3.zip | 77,968,425 | 01:39 p.m. | 06 Aug 2003 |
| | | \COEF=1e-5 \VDC=0 \Tstep=5e-4 | TStep=5e-4.zip | 76,167,277 | 01:41 p.m. | 06 Aug 2003 |
| | | \COEF=1e-5 \VDC=20 | VDC=20.zip | 77,970,684 | 01:43 p.m. | 06 Aug 2003 |
| | | \COEF=1e-5 \VDC=40 | VDC=40.zip | 77,969,945 | 01:45 p.m. | 06 Aug 2003 |
| | | \COEF=3e-4 | COEF=3e-4.zip | 77,387,889 | 01:46 p.m. | 06 Aug 2003 |
| | | \COEF=3e-5 | COEF=3e-5.zip | 76,161,532 | 01:48 p.m. | 06 Aug 2003 |
| | | \COEF=3e-6 | COEF=3e-6.zip | 76,200,673 | 01:50 p.m. | 06 Aug 2003 |
| | | \FER | FER.zip | 8,822,392 | 01:51 p.m. | 06 Aug 2003 |
| | | \No Damping | No_Damping.zip | 78,100,011 | 01:52 p.m. | 06 Aug 2003 |

NOTE: The file sizes and times may vary with operating system.

| | | | | | | |
|---|---|---|---|---|---|---|
| | | \vel5 | vel5.zip | 68,584,064 | 07:06 a.m. | 11 Aug 2003 |
| | | \vel8 | vel8.zip | 70,406,498 | 09:56 a.m. | 06 Aug 2003 |
| Compact Disc #2 | | | | | | |
| \Oblique | \Mesh1 | \FER | FER.zip | 1,317,861 | 12:43 p.m. | 06 Aug 2003 |
| | | \vel1 | vel1.zip | 15,339,365 | 12:44 p.m. | 06 Aug 2003 |
| | | \vel3 | vel3.zip | 15,400,763 | 12:45 p.m. | 06 Aug 2003 |
| | | \vel5 | vel5.zip | 15,461,115 | 12:45 p.m. | 06 Aug 2003 |
| | | \vel8 | vel8.zip | 15,789,074 | 12:46 p.m. | 06 Aug 2003 |
| | \Mesh2 | \FER | FER.zip | 2,968,790 | 12:47 p.m. | 06 Aug 2003 |
| | | \vel1 | vel1.zip | 26,357,346 | 12:48 p.m. | 06 Aug 2003 |
| | | \vel3 | vel3.zip | 26,450,749 | 12:49 p.m. | 06 Aug 2003 |
| | | \vel5 | vel5.zip | 26,514,521 | 12:49 p.m. | 06 Aug 2003 |
| | | \vel8 | vel8.zip | 26,794,508 | 12:50 p.m. | 06 Aug 2003 |
| | \Mesh3 | \FER | FER.zip | 4,663,766 | 12:51 p.m. | 06 Aug 2003 |
| | | \vel1 | vel1.zip | 37,838,927 | 12:52 p.m. | 06 Aug 2003 |
| | | \vel3 | vel3.zip | 37,935,270 | 12:53 p.m. | 06 Aug 2003 |
| | | \vel5 | vel5.zip | 38,015,300 | 12:54 p.m. | 06 Aug 2003 |
| | | \vel8 | vel8.zip | 38,315,153 | 12:55 p.m. | 06 Aug 2003 |
| | \Mesh4 | \FER | FER.zip | 6,564,291 | 01:03 p.m. | 06 Aug 2003 |
| | | \vel1 | vel1.zip | 51,491,376 | 01:04 p.m. | 06 Aug 2003 |
| | | \vel3 | vel3.zip | 51,604,321 | 01:05 p.m. | 06 Aug 2003 |
| | | \vel5 | vel5.zip | 51,701,847 | 01:07 p.m. | 06 Aug 2003 |
| | | \vel8 | vel8.zip | 52,001,265 | 01:09 p.m. | 06 Aug 2003 |
| Compact Disc #3 | | | | | | |
| \Oblique | \Mesh5 | \FER | FER.zip | 8,822,392 | 01:14 p.m. | 06 Aug 2003 |
| | | \vel1 | vel1.zip | 76,035,935 | 01:15 p.m. | 06 Aug 2003 |
| | | \vel3 | vel3.zip | 76,164,201 | 01:17 p.m. | 06 Aug 2003 |
| | | \vel5 | vel5.zip | 76,282,941 | 01:19 p.m. | 06 Aug 2003 |
| | | \vel8 | vel8.zip | 76,553,819 | 01:20 p.m. | 06 Aug 2003 |
| \Residual | | \FER | FER.zip | 3,170,753 | 01:24 p.m. | 06 Aug 2003 |
| | | \Full | full.zip | 4,222,412 | 01:25 p.m. | 06 Aug 2003 |
| | | \Half | half.zip | 4,232,304 | 01:25 p.m. | 06 Aug 2003 |
| \Shell FER | | \Mesh3 | Mesh3.zip | 30,217,490 | 01:28 p.m. | 06 Aug 2003 |
| | | \Mesh4 | Mesh4.zip | 46,662,489 | 01:29 p.m. | 06 Aug 2003 |
| | | \Mesh5 | Mesh5.zip | 72,003,146 | 01:31 p.m. | 06 Aug 2003 |
| Compact Disc #4 | | | | | | |
| \Damping | | \COEF=1e-2 | COEF=1e-2.zip | 9,173,065 | 01:35 p.m. | 06 Aug 2003 |
| | | \COEF=1e-4 | COEF=1e-4.zip | 77,574,446 | 01:37 p.m. | 06 Aug 2003 |
| | | \COEF=1e-5 \VDC=0 \TStep=1e-3 | TStep=1e-3.zip | 77,968,425 | 01:39 p.m. | 06 Aug 2003 |
| | | \COEF=1e-5 \VDC=0 \Tstep=5e-4 | TStep=5e-4.zip | 76,167,277 | 01:41 p.m. | 06 Aug 2003 |
| | | \COEF=1e-5 \VDC=20 | VDC=20.zip | 77,970,684 | 01:43 p.m. | 06 Aug 2003 |
| | | \COEF=1e-5 \VDC=40 | VDC=40.zip | 77,969,945 | 01:45 p.m. | 06 Aug 2003 |
| | | \COEF=3e-4 | COEF=3e-4.zip | 77,387,889 | 01:46 p.m. | 06 Aug 2003 |
| | | \COEF=3e-5 | COEF=3e-5.zip | 76,161,532 | 01:48 p.m. | 06 Aug 2003 |
| | | \COEF=3e-6 | COEF=3e-6.zip | 76,200,673 | 01:50 p.m. | 06 Aug 2003 |
| | | \FER | FER.zip | 8,822,392 | 01:51 p.m. | 06 Aug 2003 |
| | | \No Damping | No_Damping.zip | 78,100,011 | 01:52 p.m. | 06 Aug 2003 |

NOTE: The file sizes and times may vary with operating system.

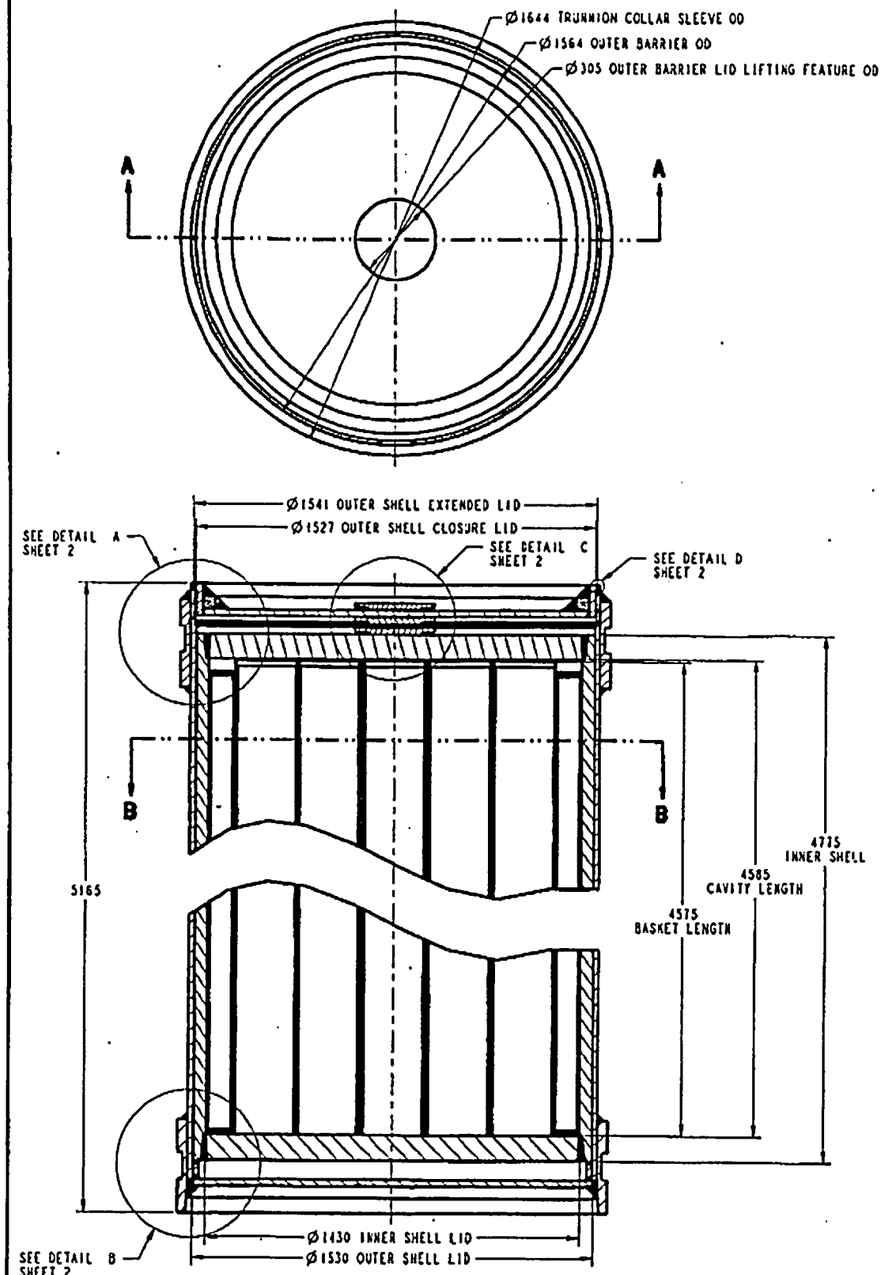


SECTION A-A

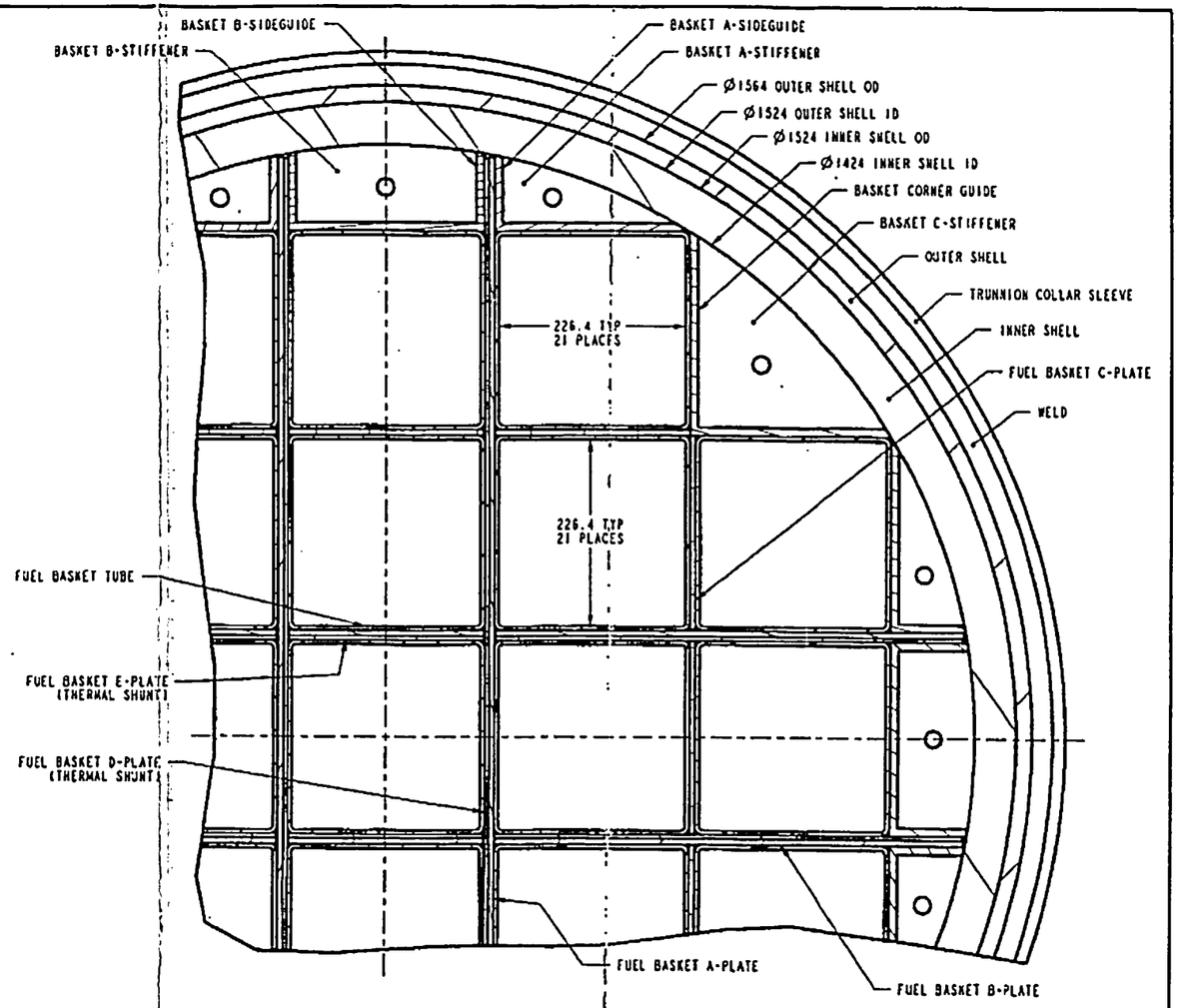


SECTION B-B

"FOR INFORMATION ONLY"

21-PWR WASTE PACKAGE CONFIGURATIONS FOR SITE RECOMMENDATION

| | |
|---|---|
| SKETCH NUMBER: | SK-0175 REV 02 SHEET 1 OF 2 |
| SKETCHED BY: | BRYAN HARKINS BH 26Jan00 |
| DATE: | 01/26/00 Title 1/26/00 1/26/00 SwB 01/26/00 |
| FILE: | /home/pro_library/checkout/sketches/21pwr/sk-0175.dwg |

UNITS: mm
DO NOT SCALE FROM SKETCH

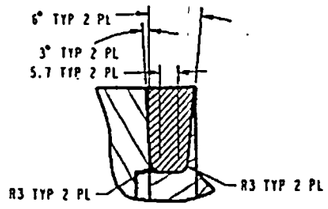


DETAIL D

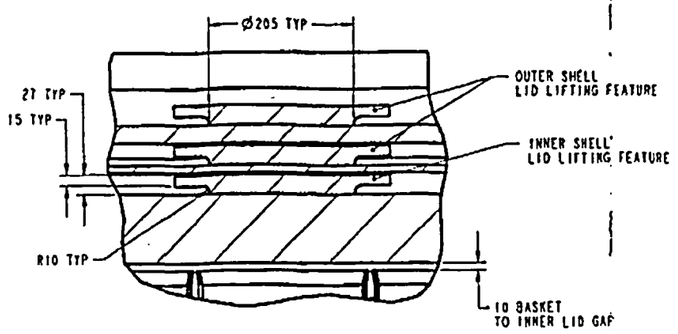


DETAIL C

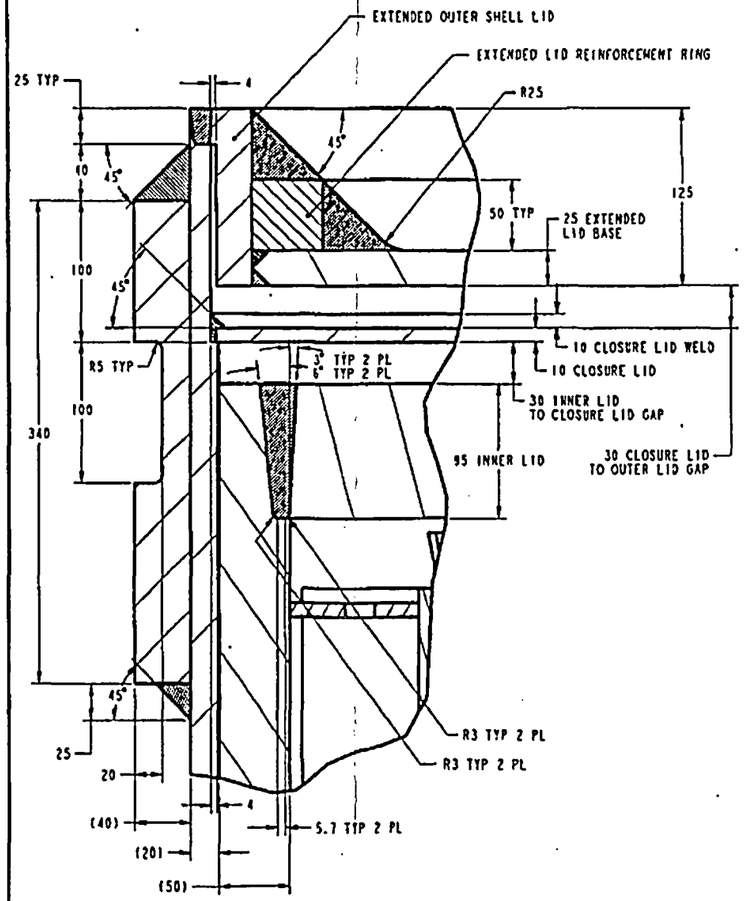


DETAIL A

21-PWR WASTE PACKAGE ASSEMBLY WITH STAINLESS STEEL/BORON PLATES

# 21-PWR CONTROL ROD WASTE PACKAGE ASSEMBLY WITH CARBON STEEL PLATES

| COMPONENT NAME | MATERIAL | THICKNESS | MASS (KG) | QTY ROD |
|---|---|---|---|---|
| BASKET A-SIDEGUIDE | SA-516 K02700 | 10 | 27 | 32 |
| BASKET A-STIFFENER | SA-516 K02700 | 10 | 0.72 | 64 |
| BASKET B-SIDEGUIDE | SA-516 K02700 | 10 | 36 | 16 |
| BASKET B-STIFFENER | SA-516 K02700 | 10 | 1.5 | 32 |
| BASKET C-STIFFENER | SA-516 K02700 | 10 | 2.3 | 32 |
| BASKET CORNERGUIDE | SA-516 K02700 | 10 | 42 | 16 |
| FUEL BASKET A-PLATE | NEUTRONIT A 978 | 7 | 85 | 8 |
| | #SA-516 K02700 | #7 | #86 | #8 |
| FUEL BASKET B-PLATE | NEUTRONIT A 978 | 7 | 85 | 8 |
| | #SA-516 K02700 | #7 | #86 | #8 |
| FUEL BASKET C-PLATE | NEUTRONIT A 978 | 7 | 44 | 16 |
| | #SA-516 K02700 | #7 | #45 | #16 |
| FUEL BASKET D-PLATE | SB-209 A96061 T4 | 5 | 21 | 8 |
| FUEL BASKET E-PLATE | SB-209 A96061 T4 | 5 | 21 | 8 |
| FUEL BASKET TUBE | SA-516 K02700 | 5 | 164 | 21 |
| INNER SHELL | SA-240 S31600 | 50 | 8709 | 1 |
| INNER SHELL LID | SA-240 S31600 | 95 | 1200 | 2 |
| INNER LID LIFTING FEATURE | SA-240 S31600 | 27 | 12 | 1 |
| OUTER SHELL | SB-575 N06022 | 20 | 4193 | 1 |
| EXTENDED OUTER SHELL LID | SB-575 N06022 | 25 | 132 | 1 |
| EXTENDED OUTER SHELL LID BASE | SB-575 N06022 | 25 | 368 | 1 |
| OUTER LID LIFTING FEATURE | SB-575 N06022 | 27 | 13 | 2 |
| EXTENDED LID REINFORCEMENT RING | SB-575 N06022 | 50 | 97 | 1 |
| OUTER SHELL FLAT CLOSURE LID | SB-575 N06022 | 10 | 159 | 1 |
| OUTER SHELL FLAT BOTTOM LID | SB-575 N06022 | 25 | 396 | 1 |
| UPPER TRUNNION COLLAR SLEEVE | SB-575 N06022 | 40 | 507 | 1 |
| LOWER TRUNNION COLLAR SLEEVE | SB-575 N06022 | 40 | 497 | 1 |
| INNER SHELL SUPPORT RING | SB-575 N06022 | 20 | 41 | 1 |
| TOTAL ALLOY 22 WELDS | SFA-5.14 N06022 | - | 249 | ** |
| TOTAL 316 WELDS | SFA-5.9 S31680 | - | 128 | ** |
| WASTE PACKAGE ASSEMBLY | - | - | 26035 | 1 |
| | - | - | #26059 | #1 |
| PWR FUEL ASSEMBLY | - | - | 773.49 | 21 |
| WP ASSEMBLY WITH SNF | - | - | 42277 | 1 |
| | - | - | #42301 | #1 |

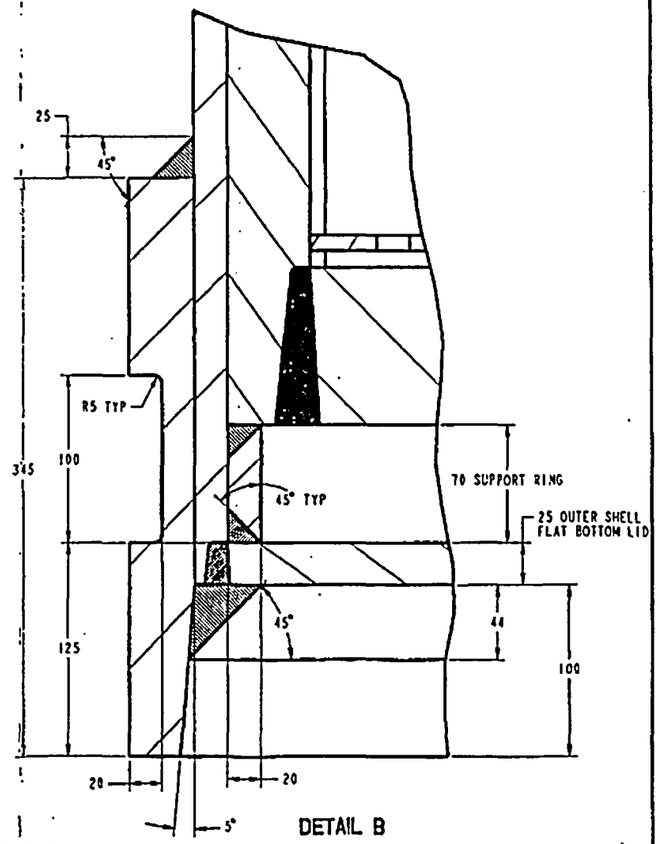


DETAIL B

* CRWMS M&O 1997. WASTE CONTAINER CAVITY SIZE DETERMINATION. BBAA00000-01717-0200-00026 REV 00. LAS VEGAS, NV: CRWMS M&O. ACC: MOL.19980106.0061

** REFER TO SK-0191 REV 00 "21-PWR WASTE PACKAGE WELD CONFIGURATION"

02 SMB 01/27/00

SK-0175 REV 01 | SHEET 2 OF 2

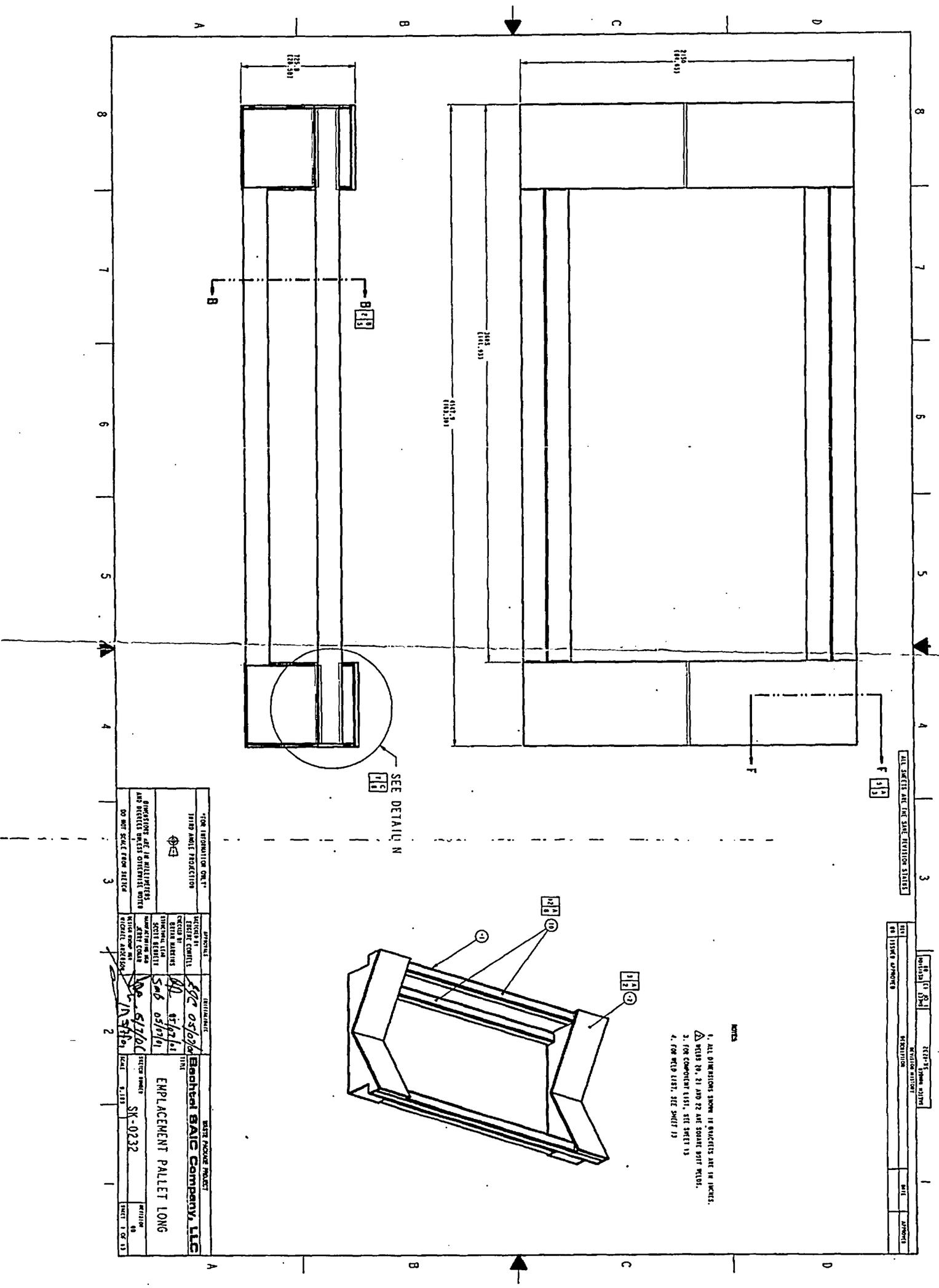
SEE DETAIL N
NOTES
1. ALL DIMENSIONS SHOWN IN BRACKETS ARE IN INCHES.
2. FOR COMPONENT LISTS, SEE SHEET 13
4. FOR WELD LIST, SEE SHEET 13
Bechtel SAIC Company, LLC
EMPLACEMENT PALLET LONG
SK-0232

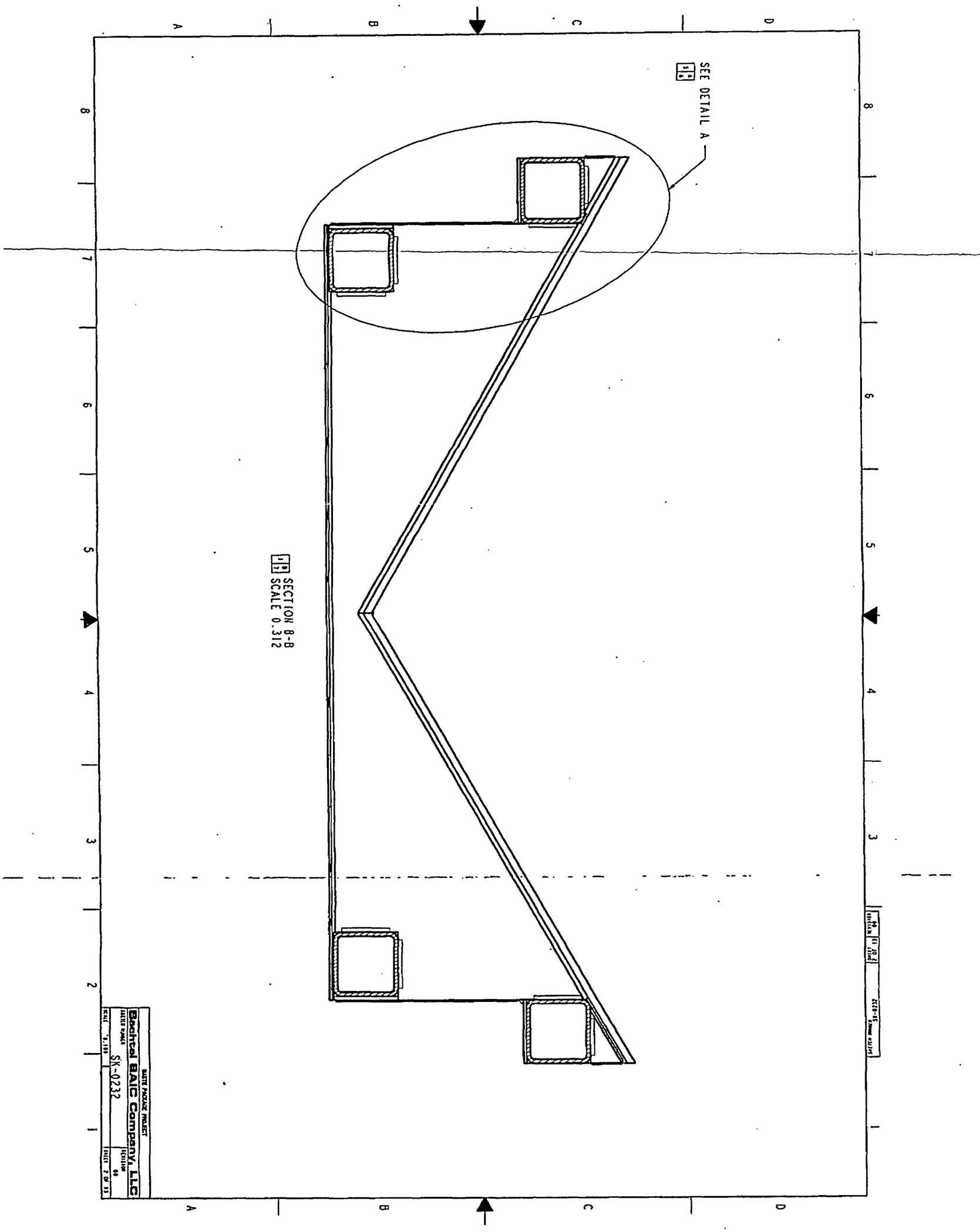
SEE DETAIL A
SECTION B-B
SCALE 0.312
Bechtel BAIC Company, LLC
SK-0232

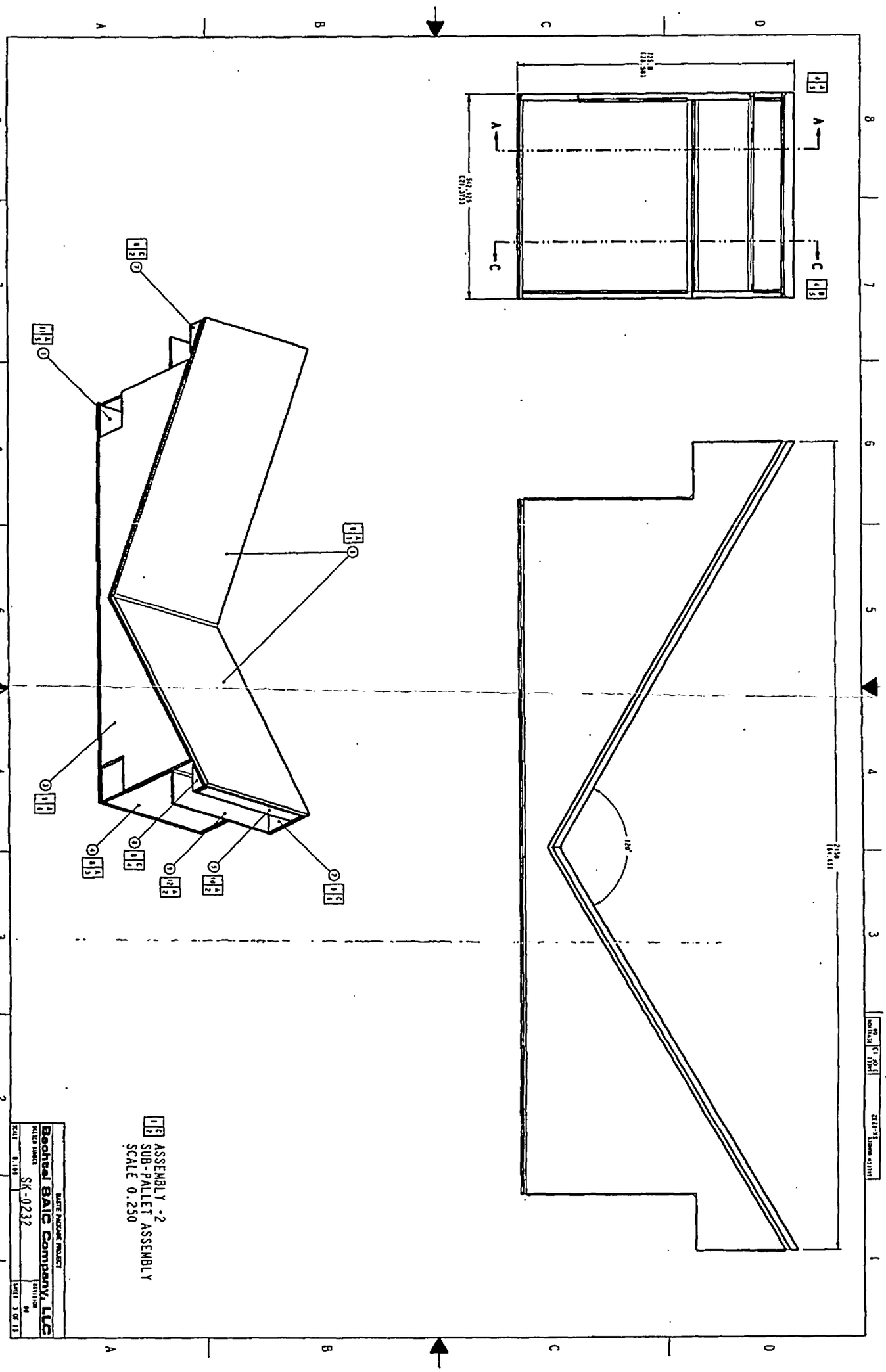
ASSEMBLY -2
SUB-PALLET ASSEMBLY
SCALE 0.250
Bechtel BAIC Company, LLC
SK-0232

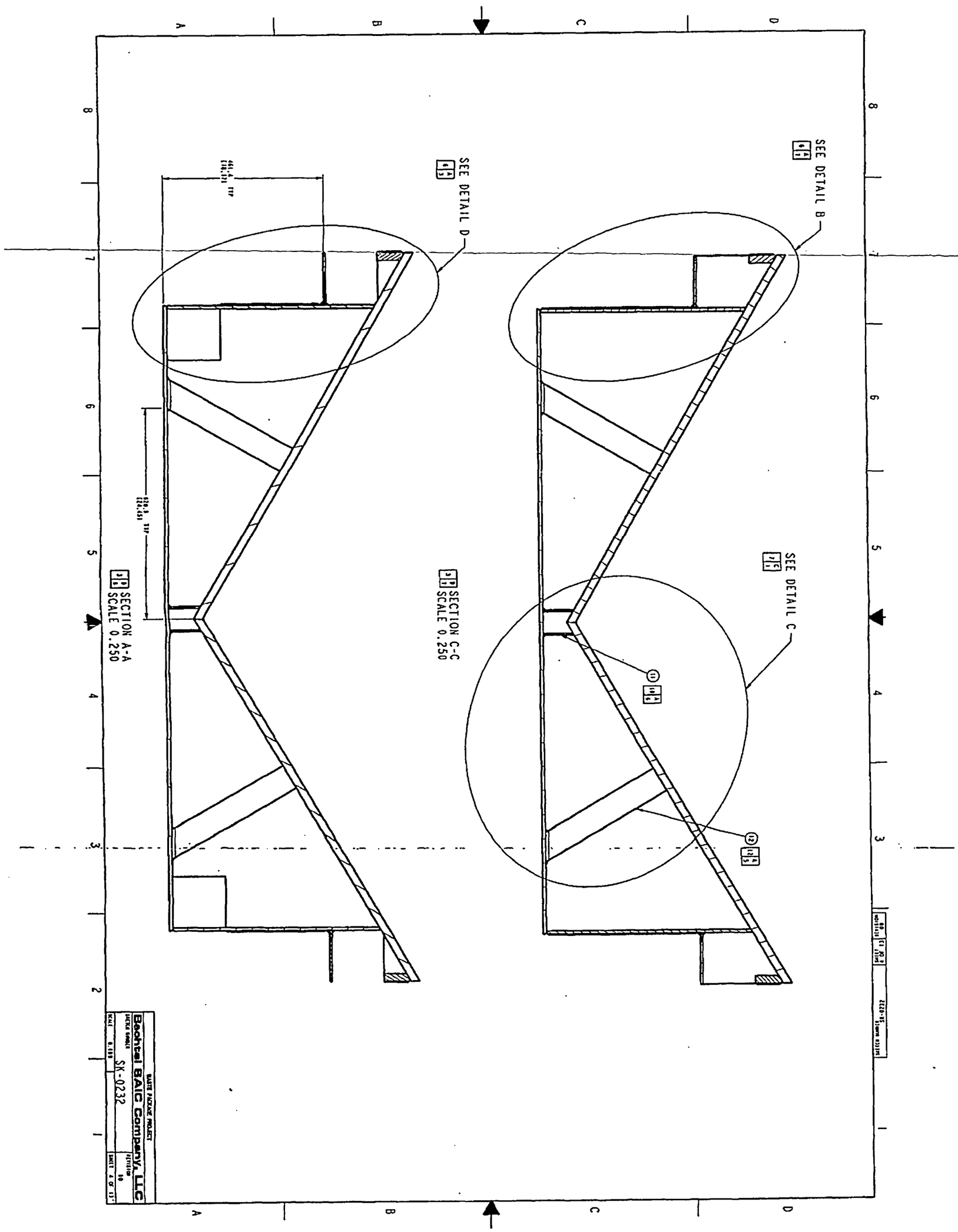
SEE DETAIL D
SEE DETAIL B
SEE DETAIL C
SECTION A-A
SCALE 0.250
SECTION C-C
SCALE 0.250
Bechtel SAIC Company, LLC
SK-0232

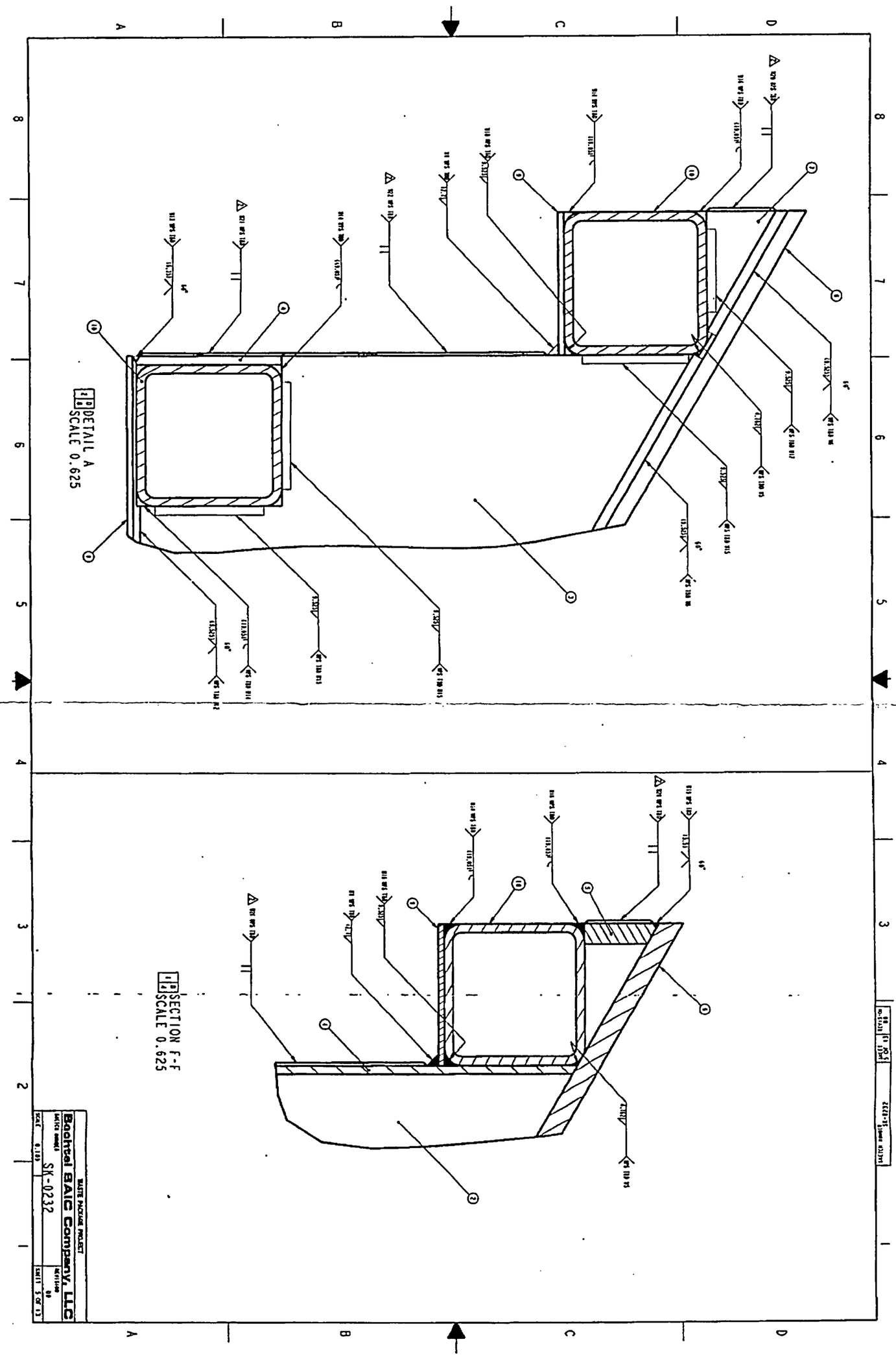
DETAIL A
SCALE 0.625
SECTION F-F
SCALE 0.625
Bechtel BAIC Company, LLC
SK-0232

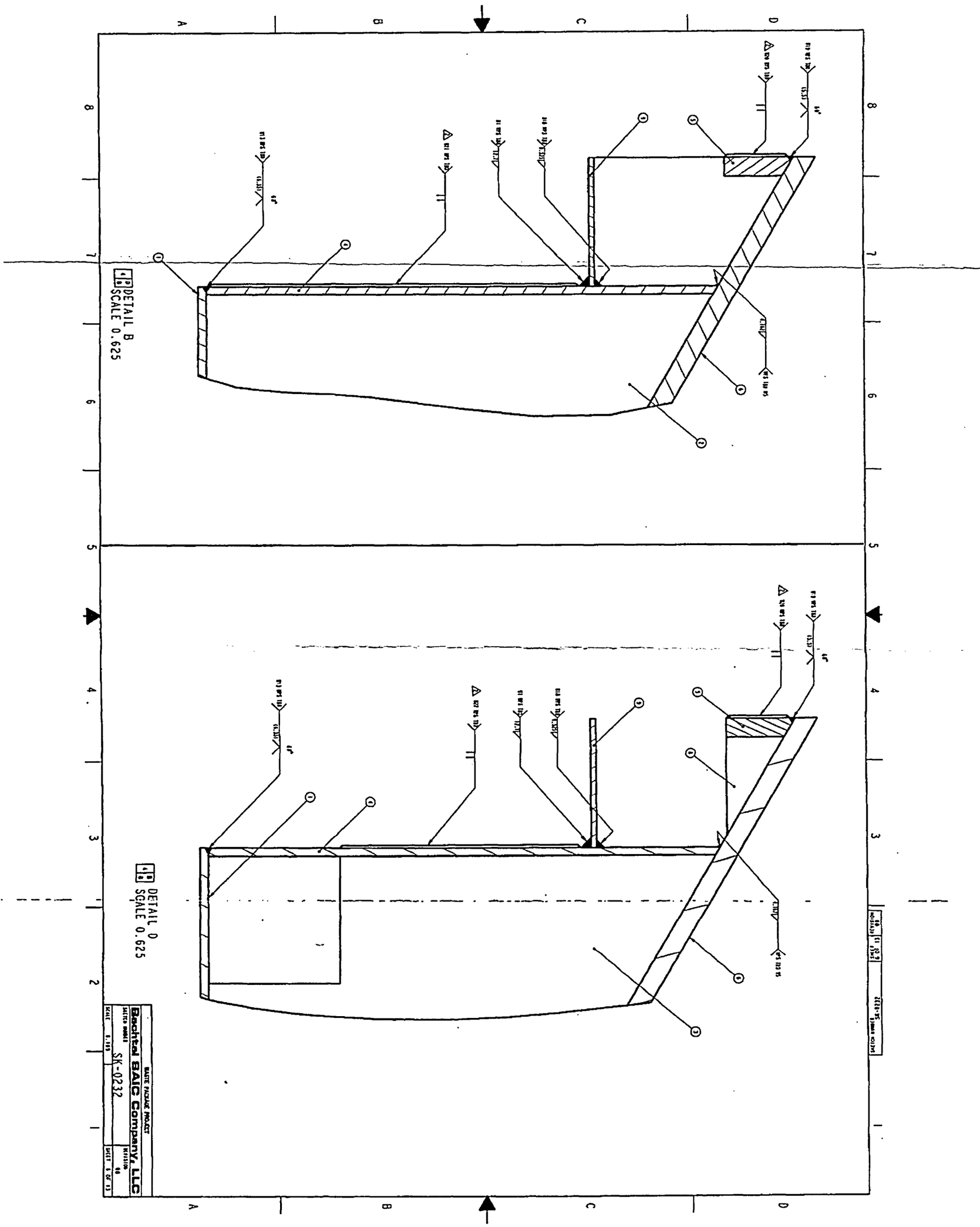
DETAIL B
SCALE 0.625
DETAIL D
SCALE 0.625
Bechtel SAIC Company, LLC
SK-0232

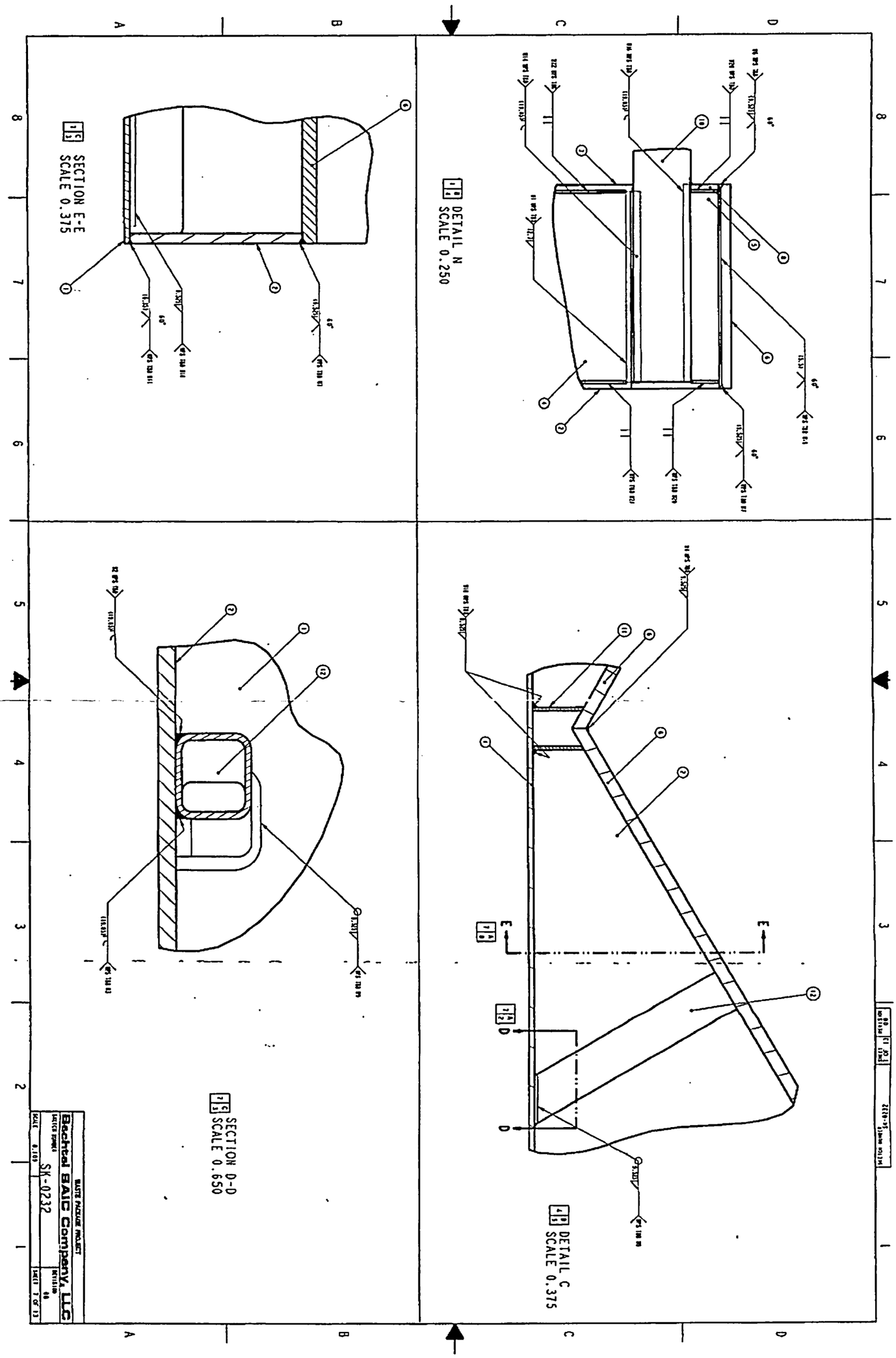
SECTION E-E
SCALE 0.375
DETAIL N
SCALE 0.250
SECTION D-D
SCALE 0.650
DETAIL C
SCALE 0.375
Bechtel BAIC Company, LLC
SK-0232

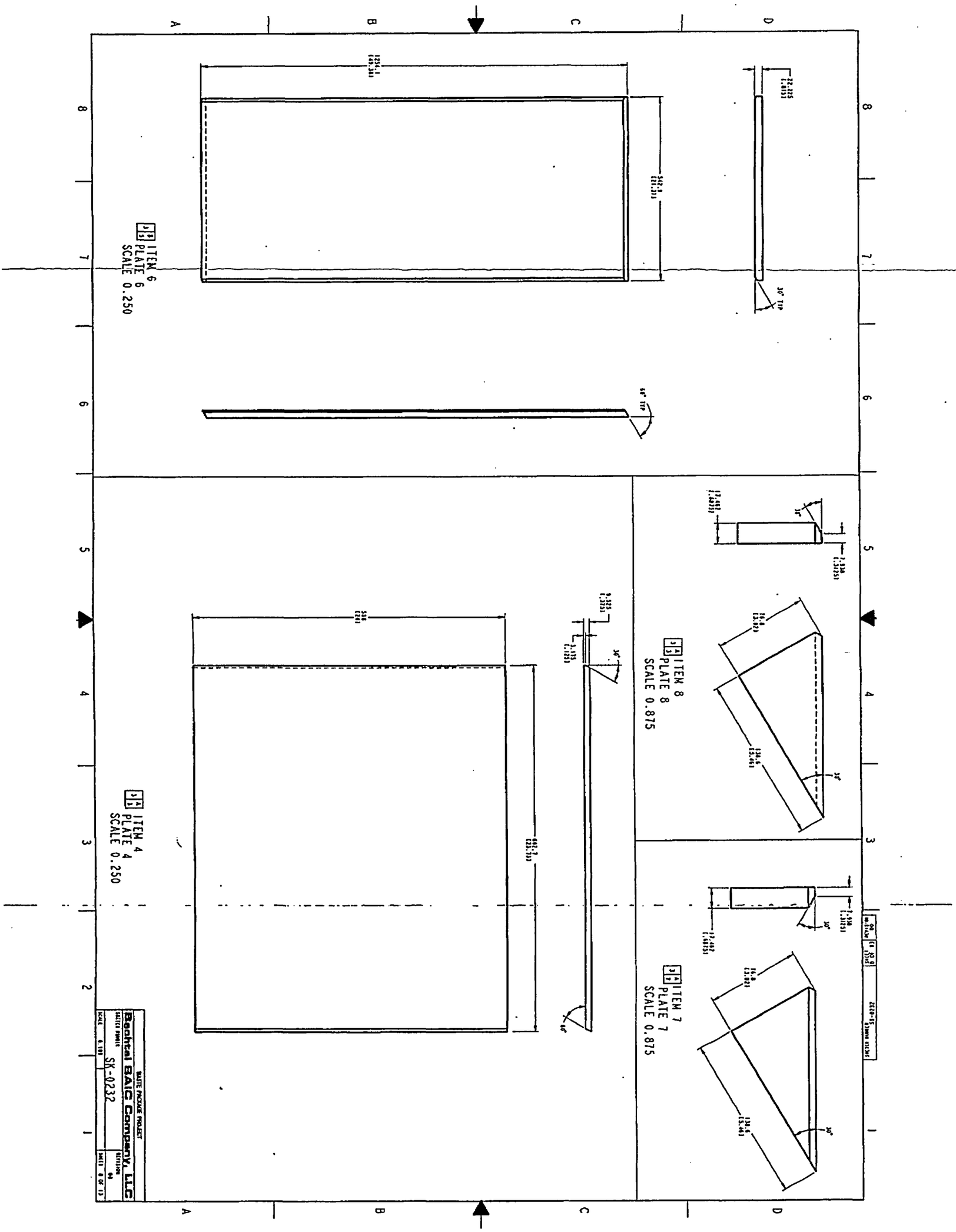
ITEM 6
PLATE 6
SCALE 0.250
ITEM 8
PLATE 8
SCALE 0.875
ITEM 4
PLATE 4
SCALE 0.250
ITEM 7
PLATE 7
SCALE 0.875
Bechtel BAIC Company, LLC
SK-0232

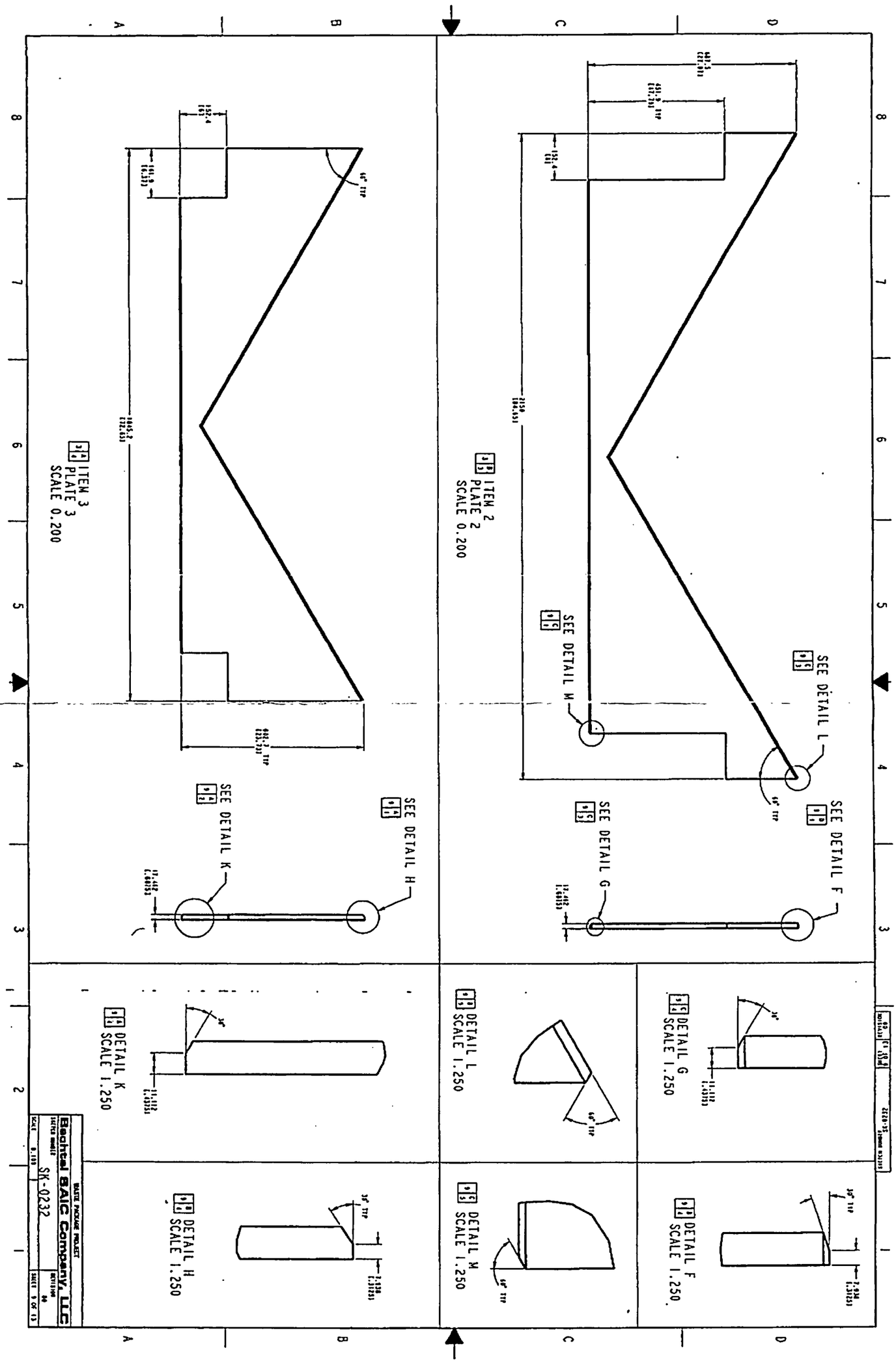
ITEM 3
PLATE 3
SCALE 0.200
ITEM 2
PLATE 2
SCALE 0.200
SEE DETAIL K
SEE DETAIL H
SEE DETAIL M
SEE DETAIL L
SEE DETAIL G
SEE DETAIL F
DETAIL K
SCALE 1.250
DETAIL L
SCALE 1.250
DETAIL G
SCALE 1.250
DETAIL H
SCALE 1.250
DETAIL M
SCALE 1.250
DETAIL F
SCALE 1.250
Bechtel SAIC Company, LLC
SK-0232

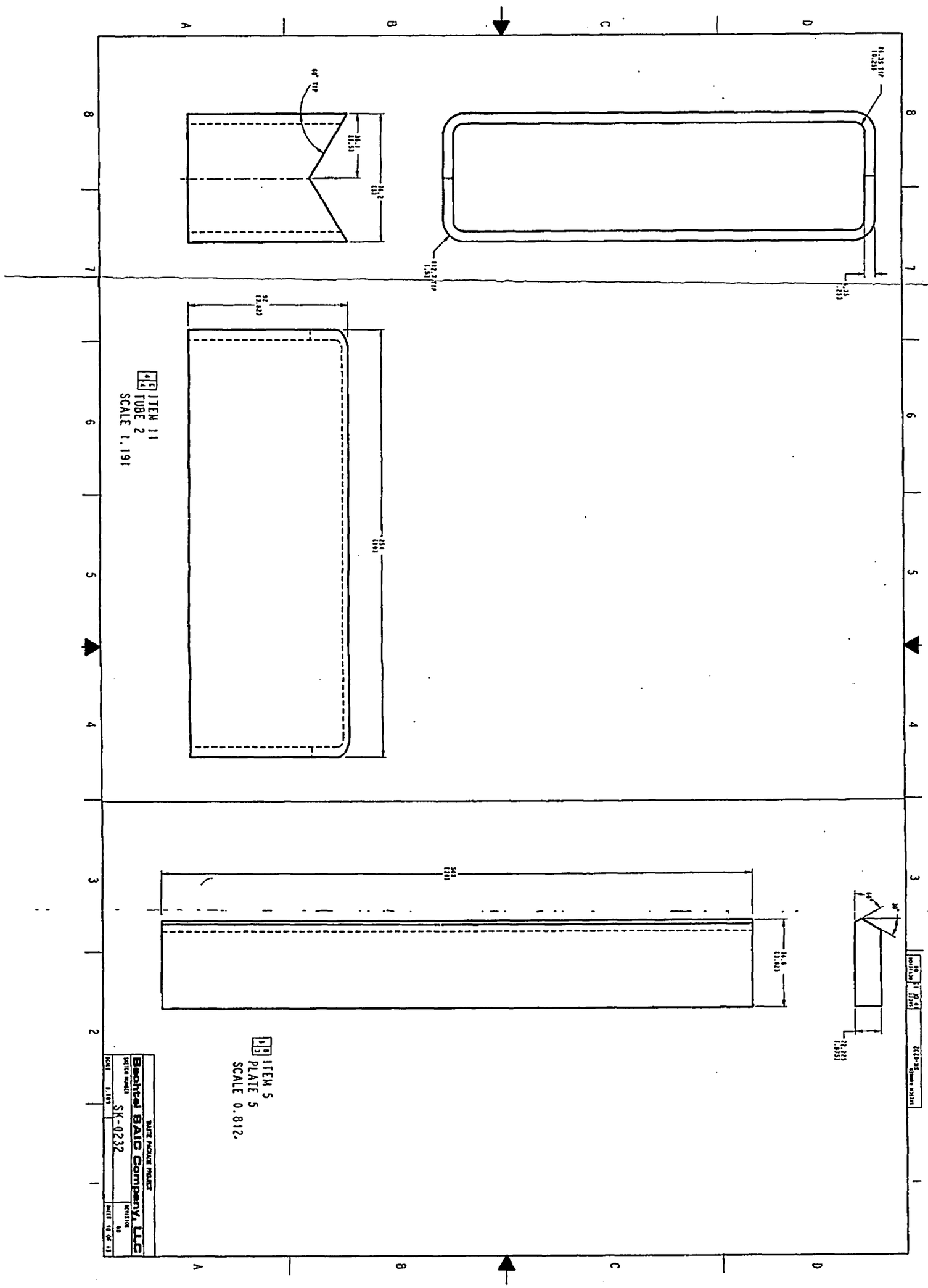
ITEM 11
TUBE 2
SCALE 1.191
ITEM 5
PLATE 5
SCALE 0.812
Bechtel SAIC Company, LLC
SK-0232

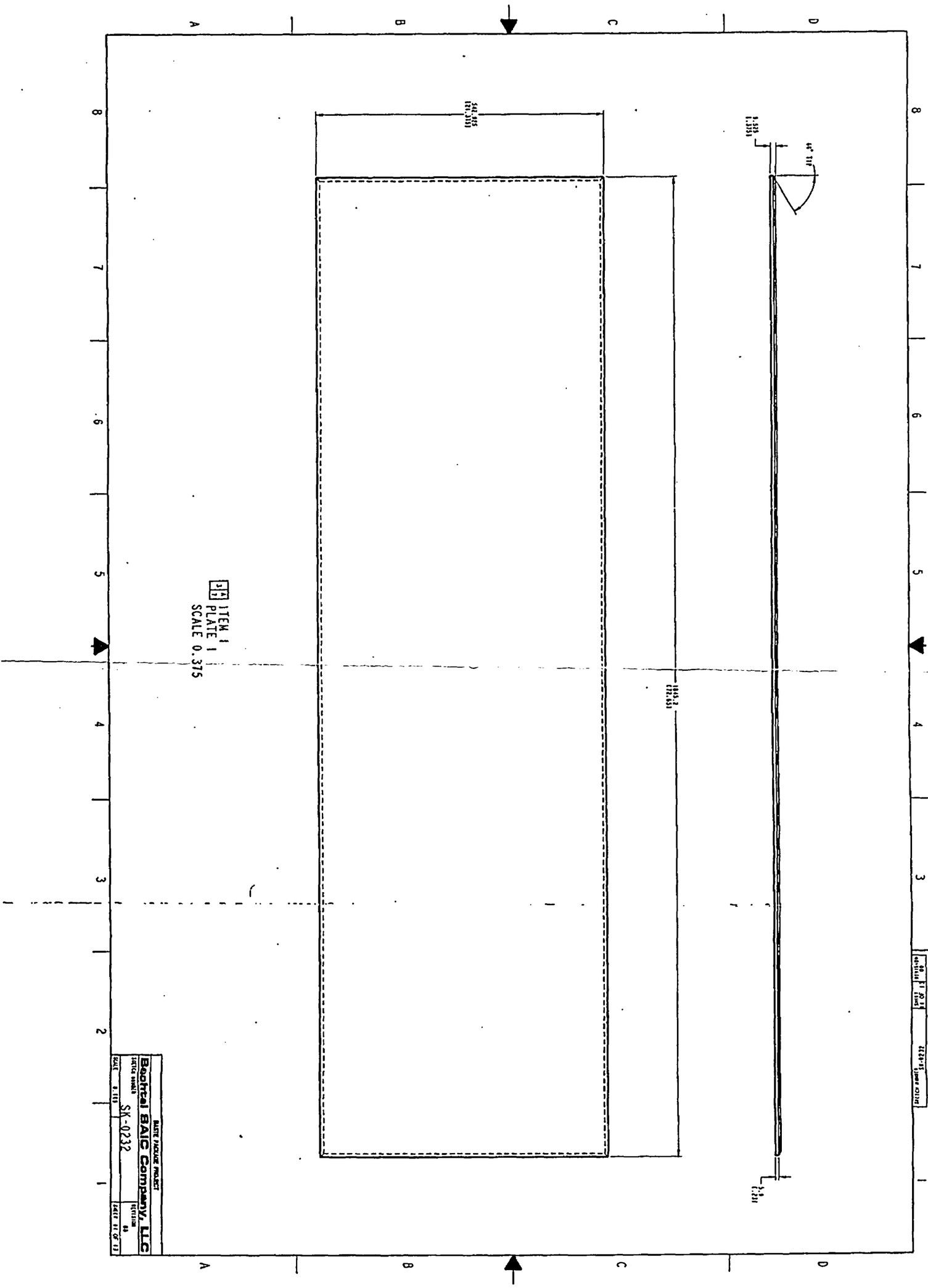
ITEM 1
PLATE 1
SCALE 0.375
Bechtel SAIC Company, LLC
SK-0232

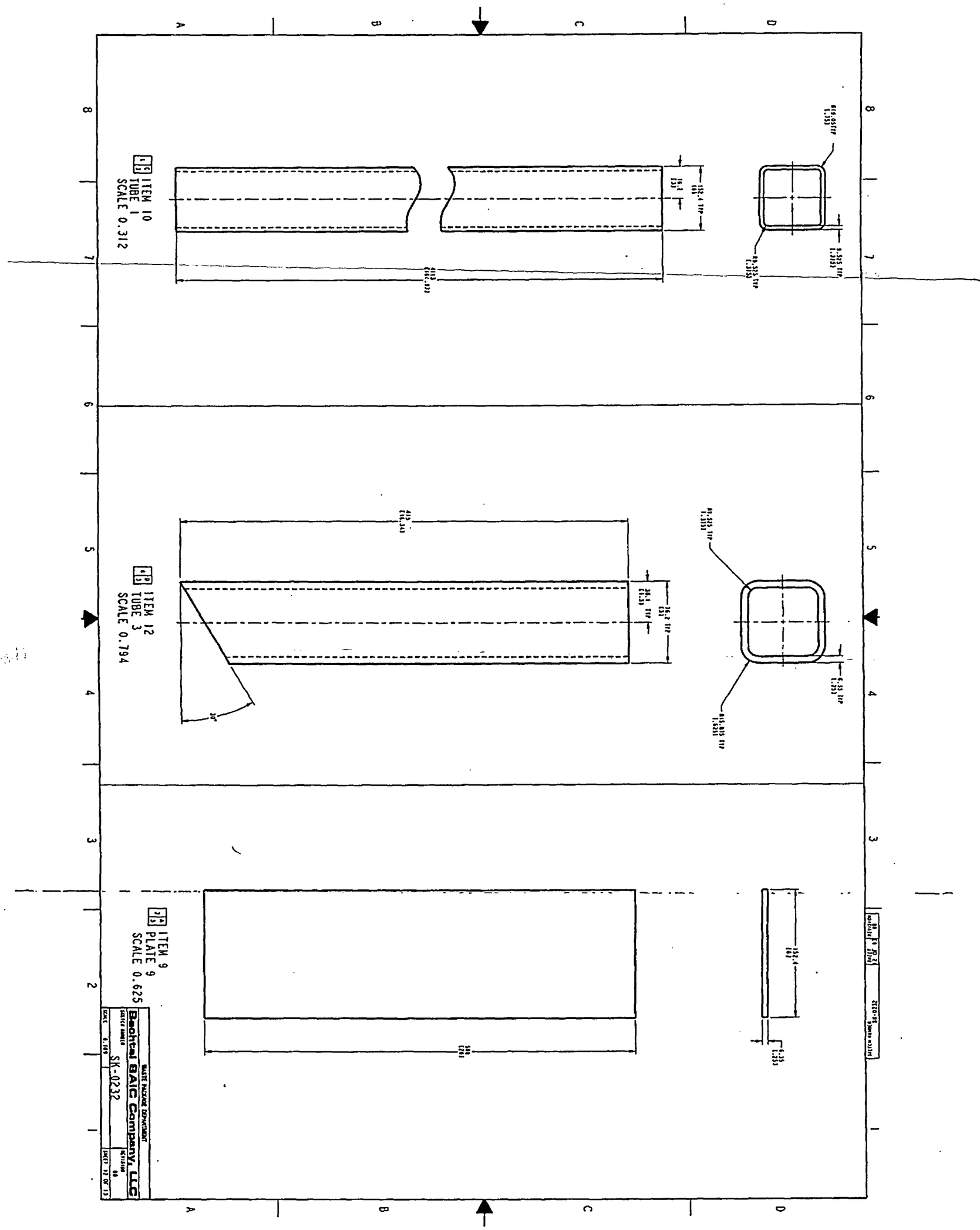
ITEM 10
TUBE 1
SCALE 0.312
ITEM 12
TUBE 3
SCALE 0.794
ITEM 9
PLATE 9
SCALE 0.625
Bechtel BAIC Company, LLC
SK-0232

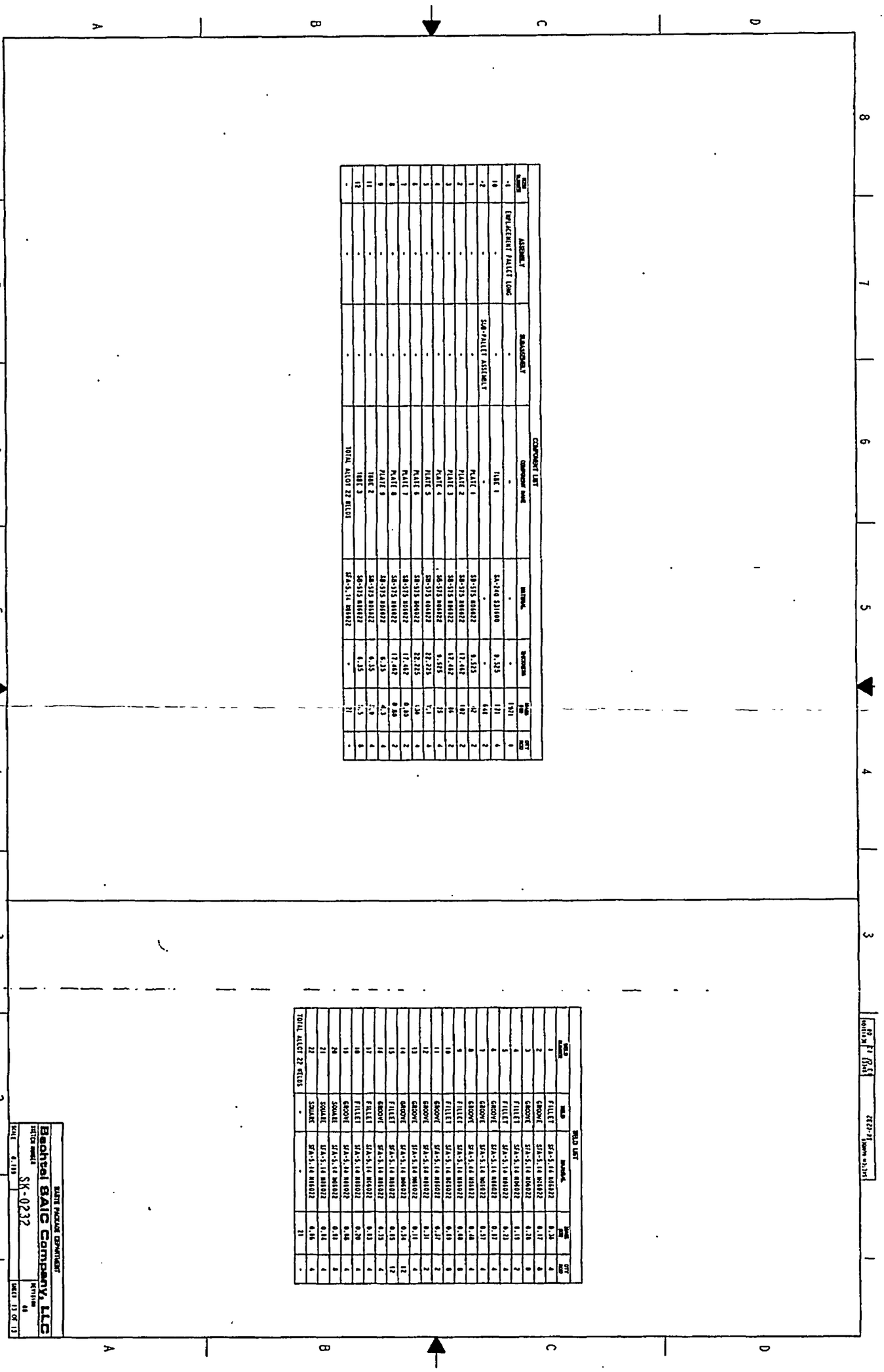

| ITEM NUMBER | ASSEMBLY | SUBASSEMBLY | COMPONENT LIST | | | | | |
|---|---|---|---|---|---|---|---|---|
| | | | COMPONENT NAME | MATERIAL | THICKNESS | MASS (KG) | QTY PER |
| -4 | EMPLACEMENT PALLET LONG | - | - | - | - | 19271 | 1 |
| -3 | - | - | TUBE 1 | SA-240 S31600 | 0.325 | 111 | 4 |
| -2 | - | SLAB+PALLET ASSEMBLY | - | - | - | 448 | 2 |
| -1 | - | - | PLATE 1 | SB-575 N06022 | 0.325 | 42 | 2 |
| 2 | - | - | PLATE 2 | SB-575 N06022 | 17.402 | 102 | 2 |
| 3 | - | - | PLATE 3 | SB-575 N06022 | 16 | 16 | 2 |
| 4 | - | - | PLATE 4 | SB-575 N06022 | 9.525 | 15 | 4 |
| 5 | - | - | PLATE 5 | SB-575 N06022 | 22.225 | 151 | 4 |
| 6 | - | - | PLATE 6 | SB-575 N06022 | 22.225 | 134 | 4 |
| 7 | - | - | PLATE 7 | SB-575 N06022 | 17.462 | 0.38 | 2 |
| 8 | - | - | PLATE 8 | SB-575 N06022 | 17.462 | 0.80 | 2 |
| 9 | - | - | PLATE 9 | SB-575 N06022 | 6.35 | 4.3 | 4 |
| 11 | - | - | TUBE 2 | SB-575 N06022 | 6.35 | 5.9 | 4 |
| 12 | - | - | TUBE 3 | SB-575 N06022 | 6.35 | 5.5 | 8 |
| - | - | - | TOTAL WEIGHT 22 WELDS | SA-240 S31600 | 6.35 | 21 | 1 |

| WELD NUMBER | WELD | MATERIAL | WELD SIZE | QTY PER |
|---|---|---|---|---|
| 1 | FILLET | SFA-5.14 N06022 | 0.34 | 4 |
| 2 | GROOVE | SFA-5.14 N06022 | 0.17 | 8 |
| 3 | GROOVE | SFA-5.14 N06022 | 0.38 | 8 |
| 4 | FILLET | SFA-5.14 N06022 | 0.19 | 2 |
| 5 | FILLET | SFA-5.14 N06022 | 0.23 | 4 |
| 6 | GROOVE | SFA-5.14 N06022 | 0.37 | 4 |
| 7 | GROOVE | SFA-5.14 N06022 | 0.48 | 4 |
| 8 | FILLET | SFA-5.14 N06022 | 0.48 | 8 |
| 9 | FILLET | SFA-5.14 N06022 | 0.19 | 8 |
| 10 | FILLET | SFA-5.14 N06022 | 0.37 | 2 |
| 11 | GROOVE | SFA-5.14 N06022 | 0.37 | 2 |
| 12 | GROOVE | SFA-5.14 N06022 | 0.31 | 2 |
| 13 | GROOVE | SFA-5.14 N06022 | 0.19 | 4 |
| 14 | GROOVE | SFA-5.14 N06022 | 0.34 | 12 |
| 15 | FILLET | SFA-5.14 N06022 | 0.19 | 12 |
| 16 | GROOVE | SFA-5.14 N06022 | 0.25 | 4 |
| 17 | FILLET | SFA-5.14 N06022 | 0.13 | 4 |
| 18 | FILLET | SFA-5.14 N06022 | 0.20 | 4 |
| 19 | GROOVE | SFA-5.14 N06022 | 0.36 | 4 |
| 20 | SQUARE | SFA-5.14 N06022 | 0.13 | 8 |
| 21 | SQUARE | SFA-5.14 N06022 | 0.14 | 4 |
| 22 | SQUARE | SFA-5.14 N06022 | 0.05 | 4 |
| TOTAL WEIGHT 22 WELDS | - | - | 31 | - |

| | | | |
|---|---|---|---|
| WASTE PACKAGE DEPARTMENT | | | |
| Bechtel SAIC Company, LLC | | | |
| SECTION VIEWS | SK-0232 | REVISION | 00 |
| SCALE 0.100 | | SHEET 11 OF 13 | |

# ATTACHMENT III

## DAMPING OF HIGH-FREQUENCY OSCILLATIONS

Application of impact load on a structure can—in absence of appropriate damping—result in nonphysical dynamic oscillations in the contact region (see Figures III-1 and III-2). These high-frequency oscillations are numerical side effects of the high strain-rate loading and can be removed by application of appropriate damping techniques.

This numerical noise often passes unnoticed since its effect on the instantaneous stress and strain measures can be negligible. On the other hand, the effective plastic strain, as a cumulative strain measure, is very sensitive to the high-frequency nodal oscillations. (A detailed discussion of the effective plastic strain is presented in Attachment IV.) The effect of the high-frequency oscillations on the effective plastic strain becomes especially pronounced with mesh refinement: the smaller the size of the typical element, the more effect the high-frequency oscillations have on the effective plastic strain. In extreme cases the effective plastic strain can be dominated by the high-frequency nodal oscillations, which can result in extremely high values of the effective plastic strain unrelated to the physics of the problem.

In order to evaluate the extent of the high frequency oscillations in the contact region it is useful to plot a high-resolution time history of the effective stress. The effective (von Mises) stress is defined as:

$$\bar{\sigma} = \frac{\sqrt{2}}{2}\left[(\sigma_1 - \sigma_2)^2 + (\sigma_2 - \sigma_3)^2 + (\sigma_3 - \sigma_1)^2\right]^{1/2}$$

where $\sigma_i \ (i = 1, 2, 3)$ are three principal stresses (Ref. 13, Chapter 3). The effective stress is convenient for this purpose since it takes into account all three principal stresses.

The event selected to study the high-frequency oscillations and their damping is the oblique drop with impact speed of $5\ m/s$. The FE representation used for this purpose is the one with the finest mesh density (i.e., Mesh 5; see Table 2 and the corresponding discussion in Section 5.2). The high-resolution time histories of the effective stress for two OCB elements in the contact region are presented in Figure III-1. The output period for this plot is $10\ \mu s$. The elements number 76231 and 76221 are characterized by the highest value of effective plastic strain before and after application of the stiffness-proportional damping, respectively. The high-resolution time histories of the effective stress presented in Figure III-1 are very noisy. Consequently, the effective plastic strain is—in absence of stiffness-proportional damping—very high (249%, see Table III-1). It is obviously necessary to apply stiffness-proportional damping in order to reduce the high-frequency nodal oscillations that contaminate the effective plastic strain.

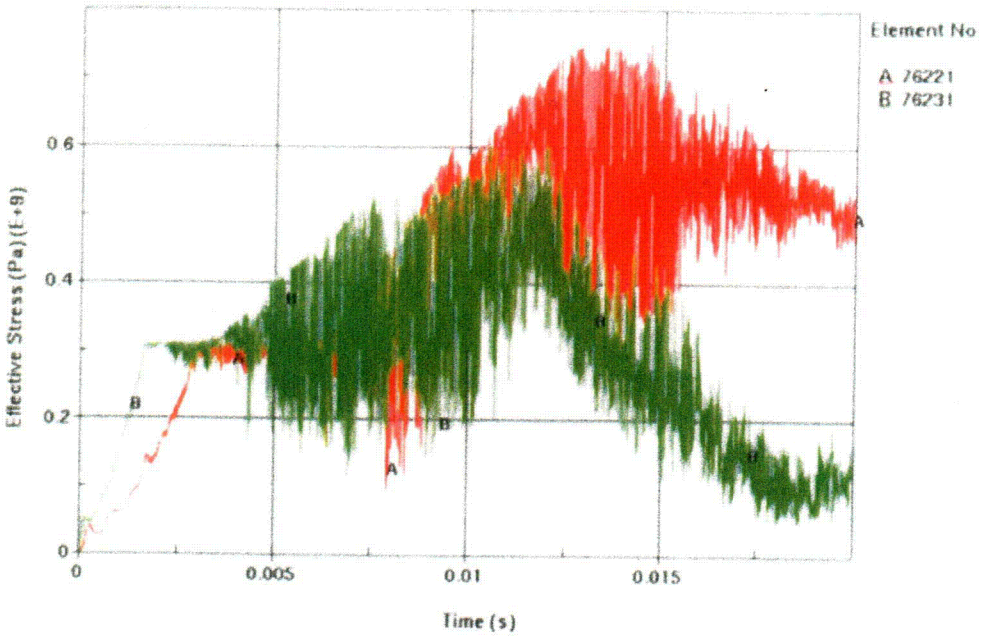


Figure III-1. Effective Stress in Elements Number 76221 and 76231 Without Damping

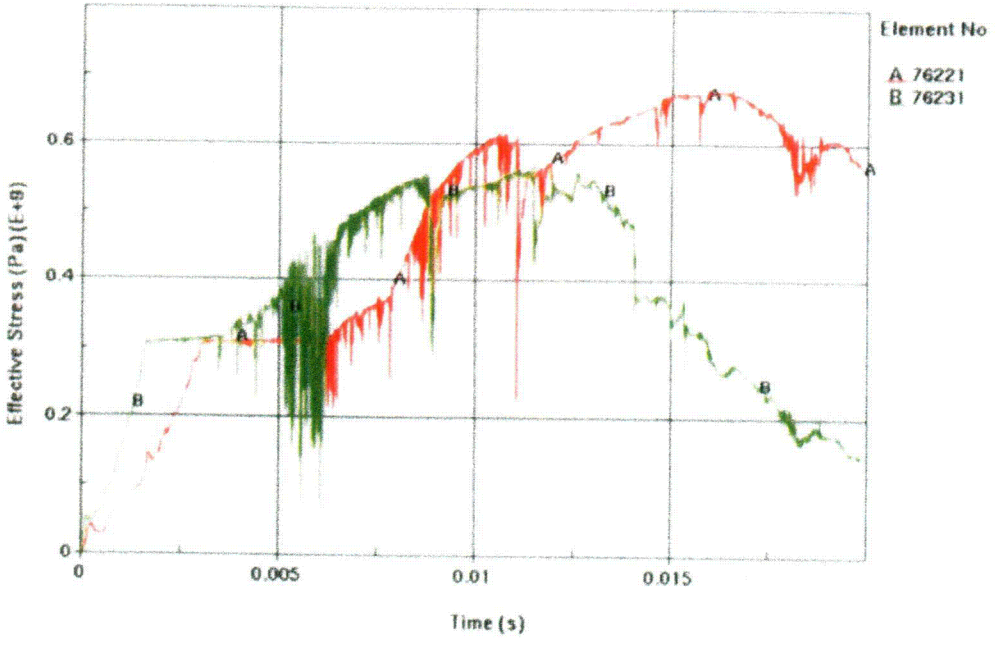


Figure III-2. Effective Stress in Elements Number 76221 and 76231 With Applied Stiffness-Proportional Damping (COEF=0.00001)



C07

Table III-1. Maximum Stress Intensity and Effective Plastic Strain for Various Levels of Stiffness-proportional Damping

| Rayleigh Damping Coefficient (COEF) | Maximum Stress Intensity (MPa) | Effective Plastic Strain (%) |
|---|---|---|
| 0 (no damping) | 895. | 249. |
| 0.0000032 | 892. | 108. |
| 0.00001 | 887. | 43.9 |
| 0.000032 | 886. | 42.9 |

The stiffness-proportional damping is an effective technique for reduction of the high frequencies. This damping is orthogonal to rigid body motion (i.e., it does not affect kinematics of the object). The stiffness-proportional damping and the selection of the Rayleigh damping coefficient (i.e., COEF) are discussed in Reference 18 (pp. 8.5 and 8.6). Although Reference 18 (p. 8.5) recommends values of the Rayleigh damping coefficient between 0.01 and 0.25, the simulations performed in this study indicate that it is not possible to reach a normal termination without a significant reduction of this coefficient. The values of the Rayleigh damping coefficient for which the stable solution is reached are presented in Table III-1.

Use of COEF=0.0001 and COEF=0.00032 results in a very slow convergence with an extremely small time step. Furthermore, the results indicate that system response is noisy as if the damping is not applied (see Attachment VIII: \Damping\COEF=1e-4\ COEF=1e-4.zip and \Damping\COEF=3e-4\ COEF=3e-4.zip). Further increase of the Rayleigh damping coefficient to, for example, 0.01 results in numerical instability (see Attachment VIII: \Damping\COEF=1e-2\ COEF=1e-2.zip). Thus, since the appropriate value for the Rayleigh damping coefficient is not easily identified (at least for solid elements with the elastoplastic material behavior), it seems necessary to determine the coefficient by iterative procedure on a case-by-case basis.

The results of the iterative determination of the Rayleigh damping coefficient are presented in Table III-1. (Note that all results presented in Table III-1 are obtained by using the output period of $5 \cdot 10^{-4}$ $s$.) The use of COEF=0.00001 results in a significant reduction of the high-frequency response as demonstrated in Figure III-2. Consequently, the effective plastic strain is reduced more than five times (Table III-1). Further increase of the Rayleigh damping coefficient to 0.000032 results in a minor reduction of the effective plastic strain previously reached for COEF=0.00001. On the other hand, a decrease of the Rayleigh damping coefficient to 0.0000032 results in a significant increase of the effective plastic strain.

Thus, it seems reasonable to claim that the stable solution is reached regarding the effective plastic strain for either COEF=0.00001 or COEF=0.000032. Note that the maximum stress intensity does not change significantly regardless of the applied damping level (including "no damping" as a limit case). Consequently, the Rayleigh damping coefficient of 0.00001 is used throughout this analysis since it ensures that the effective plastic strain is not highly noise-sensitive.

It is important to recognize that it may be possible to improve the stability of results for the higher values of the Rayleigh damping coefficient by significant reduction of the time step size. This

alternative is not explored herein since the results are sufficiently stable (regarding the high-frequency oscillations) for the objective of this study.

It should also be recognized that further reduction of the high-frequency oscillations in the contact region is possible by applying a viscous damping in the contact definition. The original intent of the viscous contact damping was to reduce oscillations normal to the contact surfaces during metal forming simulations; however, it was later found to work effectively in reduction of the high-frequency oscillations in problems involving impact (Ref. 17, Section 23.8.5).

The viscous damping coefficient (VDC) is defined in percent of critical (see Ref. 18, p. 6.10). Two values are used herein: 20 and 40. The results of this inquiry are presented in Table III-2 and Figures III-3 and III-4. (All these results are obtained from simulations performed with a Rayleigh damping coefficient of 0.00001 and an output period of 0.001 $s$.)

Table III-2. Maximum Stress Intensity and Effective Plastic Strain for Various Levels of Viscous Contact Damping

| Viscous Damping Coefficient (VDC) | Maximum Stress Intensity (MPa) | Effective Plastic Strain (%) |
|---|---|---|
| 0 (no damping) | 877. | 44.2 |
| 20 | 872. | 43.0 |
| 40 | 873. | 42.9 |

By comparing the high-resolution time histories of the effective stress obtained without (Figure III-2) and with (Figure III-3 and III-4) viscous contact damping, it can be observed that the viscous contact damping indeed reduces the remaining high-frequency noise to a certain extent. Also, by comparing results obtained for two different viscous damping coefficients, VDC=20 (Figure III-3) and VDC=40 (Figure III-4), it can be concluded that the increase in viscous damping coefficient results in slight reduction of the high-frequency noise.

However, the effect of the viscous contact damping on the maximum stress intensity and the effective plastic strain is more important for this study than the qualitative description of the high-frequency noise in the stress time histories. According to the results presented in Table III-2, the difference in the maximum stress intensity is negligible (less than one percent). The difference in the effective plastic strain is slightly more pronounced with the maximum difference smaller than three percent. It should be noted that if the stiffness-proportional damping is not applied the contact viscous damping significantly reduces the computational noise.

Finally, the maximum stress intensity for the $5-m/s$ oblique drop is evaluated by using two different output periods. The maximum stress intensities for the output period of 0.001 $s$ and 0.0005 $s$ are 877 $MPa$ and 887 $MPa$, respectively. The relative difference of approximately 1 percent indicates that the output period of 0.001 $s$ is sufficiently small. The output time period of 0.001 $s$ is, therefore, used consistently in all calculations presented in this document.

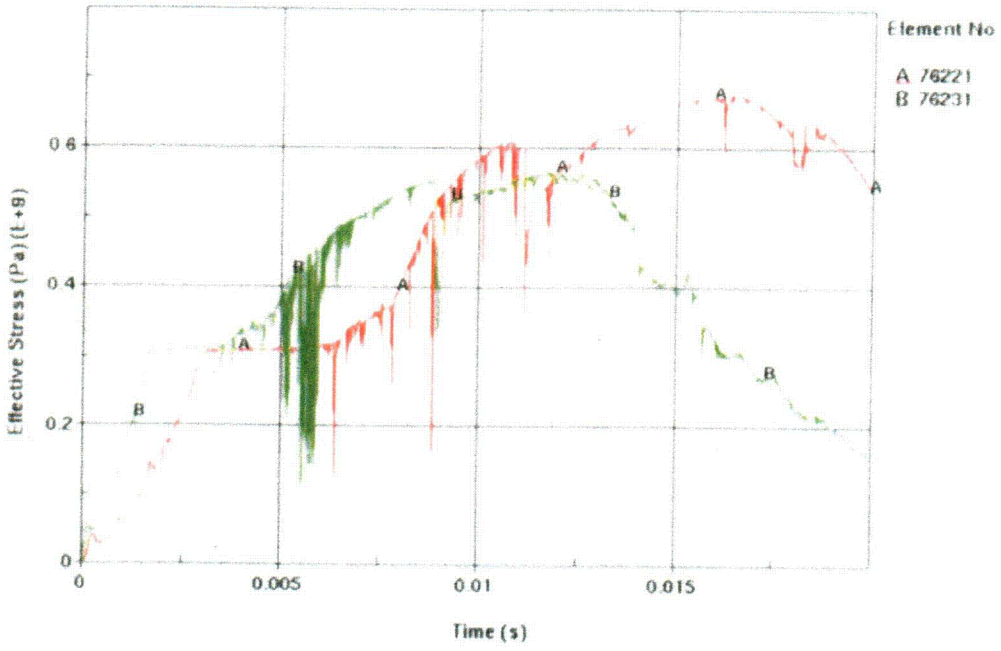


Figure III-3. Effective Stress in Elements Number 76221 and 76231 With Applied Stiffness-Proportional Damping (COEF=0.00001) and Viscous Contact Damping (VDC=20)

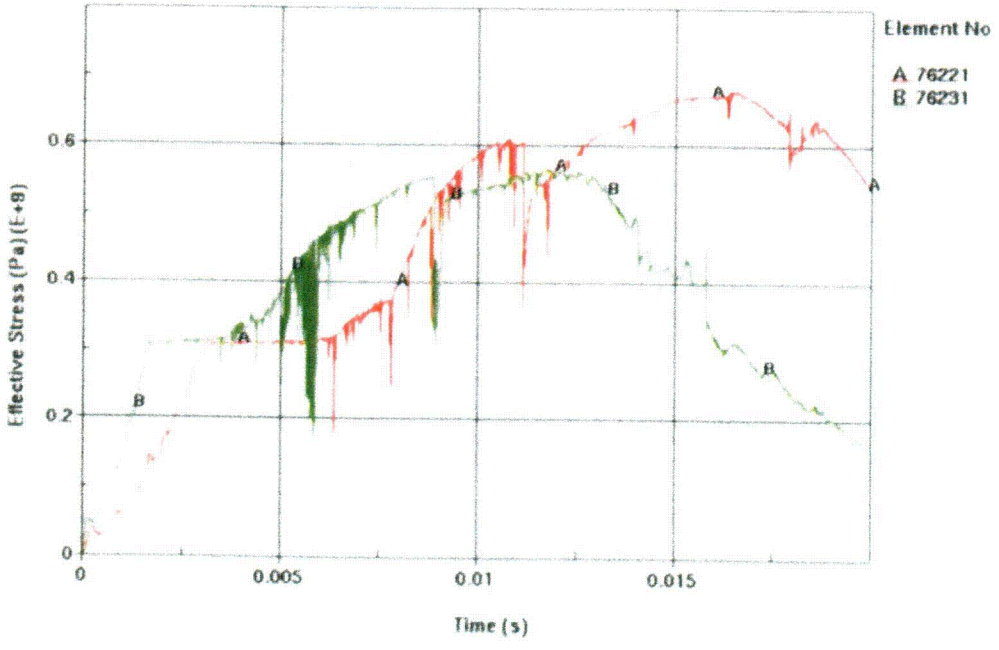


Figure III-4. Effective Stress in Elements Number 76221 and 76231 With Applied Stiffness-Proportional Damping (COEF=0.00001) and Viscous Contact Damping (VDC=40)



C08

# ATTACHMENT IV

## EFFECTIVE PLASTIC STRAIN

The effective (equivalent) plastic strain, presented in this attachment, is defined as:

$$\bar{\varepsilon} = \int_0^t \left( \frac{2}{3} \dot{\varepsilon}_{ij}^{p} \, \dot{\varepsilon}_{ij}^{p} \right)^{1/2} dt$$

where $\dot{\varepsilon}_{ij}^{p}$ is plastic strain rate tensor (see Ref. 17, p. 16.11), $t$ is time, and repeated indices imply summation.

The effective plastic strain is a hardening parameter that, similar to plastic work, provides a measure of plastic distortion. It is a cumulative, non-decreasing strain measure that takes into account the entire deformation history. Since the driving mechanism for plastic distortion is the transformation of the externally supplied energy (for example, kinetic energy in case of impacts and drops) into plastic work, the effective plastic strain offers better indication of the material condition than any instantaneous stress (or strain) measure. (For detailed discussion of strain hardening and related issues see Reference 20, Chapter II, Section 3.)

If a specimen of an isotropic material, characterized by plastic incompressibility, is subjected to a uniaxial tensile (or compressive) test, the effective plastic strain reduces to the true strain. This provides an important link between three-dimensional state of stress, dominating engineering practice, and one-dimensional state of stress characterizing (until necking) the uniaxial tensile test.

Unfortunately, as a cumulative strain measure, the effective plastic strain is extremely sensitive to any "numerical noise" during simulation (see Table III-1). Even the slightest erratic motion of only a few nodes, that is very often difficult (and unnecessary) to suppress completely, during the impact simulation can cause unphysical buildup of the effective plastic strain. (Most of the time this noise does not have significant effect on instantaneous stress and strain measures [as indicated in Table III-1].) This adverse effect of a minuscule erratic nodal motion on the effective plastic strain becomes more pronounced as the typical element size is reduced (since the volume or the area over which the strain is averaged is smaller) as indicated in Tables IV-1 and IV-2.

The maximum effective plastic strains reached during the horizontal and oblique drops of the WP on the pallet are presented in Table IV-1 and Table IV-2, respectively, for four different impact speeds. The evaluated FE representations are described in Section 5.2.

Table IV-1 Maximum Effective Plastic Strain for Horizontal Drop

| Impact Speed (m/s) | Effective Plastic Strain (%) | | | |
|---|---|---|---|---|
| | Mesh 1 | Mesh 2 | Mesh 3 | Mesh 4 |
| 1 | 0.8 | 3.7 | 4.8 | 5.9 |
| 3 | 2.5 | 9.0 | 11.0 | 15.9 |
| 5 | 3.5 | 21.6 | 27.3 | 33.5 |
| 8 | 3.8 | 30.3 | 40.3 | 50.7 |

Table IV-2 Maximum Effective Plastic Strain for Oblique Drop

| Impact Speed (m/s) | Effective Plastic Strain (%) | | | | |
|---|---|---|---|---|---|
| | Mesh 1 | Mesh 2 | Mesh 3 | Mesh 4 | Mesh 5 |
| 1 | 1.8 | 8.0 | 8.4 | 9.4 | 13.0 |
| 3 | 3.3 | 15.9 | 21.2 | 23.7 | 27.7 |
| 5 | 4.4 | 29.2 | 42.2 | 49.2 | 61.5 |
| 8 | 4.8 | 41.4 | 58.2 | 69.0 | 86.8 |

According to the results presented in Tables IV-1 and IV-2 it can be concluded that the discussion of the stress-intensity results (Section 6.2) is applicable to the effective-plastic-strain results as well. Furthermore, the results presented in Tables IV-1 and IV-2 suggest that is difficult to achieve local convergence of the effective plastic strain, even with extremely high in-plane mesh density, as long as the number of solid-element layers across the wall thickness is four. On the other hand, it is known that for the locally evaluated (i.e., at one integration point) effective plastic strain, mesh refinement leads to results which can change significantly for mesh to mesh (Ref. 18, p. 15 [MAT]). It is obvious that element size and shape strongly affects the effective plastic strain. In the case of a coarse mesh the effective plastic strain is "smeared" over a large element volume and the strain estimates are unreliable (see results for Mesh 1 in Tables IV-1 and IV-2). The results presented in Tables IV-1 and IV-2 also suggest that in the cases of very localized loading of a structure (resulting in localized deformations such as, as an example, dent) the locally evaluated effective plastic strain should be used judiciously and warily (if at all) for failure assessment.[2]

[2] This problem is addressed by nonlocal evaluation of the effective plastic strain (or in more general sense by nonlocal failure theories). In the case of the nonlocal approach, the value of effective plastic strain depends on the state of the material within a radius of influence that surrounds the integration point (see Ref. 18, p. 15 [MAT]). This radius of influence typically surrounds a large number of elements. An advantage of nonlocal evaluation of effective plastic strain is that the mesh sensitivity of results is significantly reduced. A major disadvantage of this approach is that "the radius of influence"—that strongly affects results—is not easy to determine objectively.

# ATTACHMENT V

## DAMAGED AREA BASED ON STRESS INTENSITY

The area of the WP OCB where the residual stress intensity exceeds the stress limit (see Section 1 and Assumption 3.9) is, throughout this attachment only, referred to as "the damaged area." The purpose of this evaluation is to explore the effect of using the alternative stress measure (that takes into account triaxiality of stress state) in evaluation of the damaged area. Damaged areas for horizontal and oblique drops are presented in Tables V-1 and V-2, respectively.

Table V-1. Damaged Area for Horizontal Drop

| Impact Speed (m/s) | Damaged Area ($\times 10^{-3}$ $m^2$) (80% criterion / 90% criterion) | | | |
|---|---|---|---|---|
| | Mesh 1 | Mesh 2 | Mesh 3 | Mesh 4 |
| 1 | 8.73 / 4.39 | 1.28 / 0 | 5.01 / 0.55 | 4.61 / 0.43 |
| 3 | 5.81 / 0 | 0.73 / 0 | 0.71 / 0 | 0.60 / 0.03 |
| 5 | 3.65 / 0 | 2.62 / 0.31 | 4.81 / 0 | 3.35 / 0.17 |
| 8 | 66.44 / 31.88 | 18.86 / 1.67 | 14.52 / 1.04 | 17.54 / 1.46 |

Table V-2. Damaged Area for Oblique Drop

| Impact Speed (m/s) | Damaged Area ($\times 10^{-3}$ $m^2$) (80% criterion / 90% criterion) | | | | |
|---|---|---|---|---|---|
| | Mesh 1 | Mesh 2 | Mesh 3 | Mesh 4 | Mesh 5 |
| 1 | 10.83 / 7.21 | 13.48 / 8.90 | 14.02 / 8.26 | 15.22 / 8.74 | 14.53 / 8.15 |
| 3 | 28.12 / 14.36 | 6.98 / 1.42 | 6.86 / 1.61 | 4.98 / 0.97 | 4.64 / 1.41 |
| 5 | 36.12 / 25.29 | 14.45 / 6.02 | 71.74 / 59.65 | 15.27 / 5.38 | 12.64 / 5.40 |
| 8 | 20.97 / 7.96 | 19.35 / 3.64 | 16.56 / 5.08 | 15.86 / 5.53 | 18.94 / 5.20 |

The damaged area based on stress intensity exceeds the damaged area base on the 1st principal stress (Tables 5 and 6). Nonetheless, the previous observation—that the damaged area is the largest for the coarsest mesh (Mesh 1)—still holds with only a few exceptions.

# ATTACHMENT VI

## SHELL-ELEMENT FE REPRESENTATION

The purpose of this attachment is to study the effect of using shell elements for the FE representation of the OCB in this calculation (see Figure VI-1). The parameters characterizing the three FE representations used for this purpose and the results obtained are presented in Table VI-1. Note that the area of typical element in the finest shell FE representation (i.e., Mesh 5) is similar to the area of typical element in the finest solid FE representation (also designated as Mesh 5; see Table 2 and Table VI-2). Five integration points across the OCB thickness are used for all shell-element FE representations.

The FE representations are then used in LS-DYNA V960.1106 to perform a transient dynamic analysis of the WP impacting the pallet. The selected drop is the oblique drop with initial velocity of 3 *m/s*.

Table VI-1. Parameters and Results for Three Different Shell FE Representations

| | Mesh 3 | Mesh 4 | Mesh 5 |
|---|---|---|---|
| Typical Element Number / Area ($mm^2$) | 41510 / 87.6 | 48540 / 39.0 | 59439 / 21.9 |
| CPU Time (days per second of physical time) | 14.5 | 32.2 | 84.1 |
| Damaged Area ($\times 10^{-3}$ $m^2$) (80% criterion / 90% criterion) | 6.13 / 1.99 | 4.67 / 1.64 | 5.05 / 0.75 |
| Maximum Stress Intensity (MPa) | 539. | 721. | 1073. |
| Maximum Effective Plastic Strain (%) | 17.0 | 26.3 | 63.4 |

According to the results presented in Table VI-1 the damaged area is a fast-converging parameter of state. On the other hand, the mesh refinement from Mesh 4 to Mesh 5 results in an unacceptable difference in the maximum stress intensity and the maximum effective plastic strain.

The comparison of the results obtained by using the shell-element FE representation and the solid-element FE representation (Mesh 5) can be made based on the results presented in Table VI-2. (Note that two representations designated as Mesh 5 have a similar in-plane area [see Table VI-2].)

The first observation that can be made based on the results presented in Table VI-2 is that the shell-element FE representation (Mesh 5) is not computationally more economic than the solid-element FE representation with comparable in-plane area. The benefit of using fewer elements in the finely meshed region of shell-element FE representation (compared to the solid-element counterpart) is made ineffective by the increase of elements in other regions. In other words, the transition from the finely meshed region to the coarsely meshed region of the OCB by using the tied interface contact (in the solid-element FE representation; see Figures 2, 3, and 4) is much more efficient than the gradual coarsening of the mesh (see Figure VI-1) that is necessary in the shell-element FE representation.